

The Pennsylvania State University

The Graduate School

College of Engineering

**PARTICLE IMAGE VELOCIMETRY MEASUREMENTS OF FLOW IN AN
ANATOMICALLY-ACCURATE SCALED MODEL OF THE RODENT NASAL CAVITY**

A Thesis in

Aerospace Engineering

by

Christopher Rumpel

© 2014 Christopher Rumpel

Submitted in Partial Fulfillment
of the Requirements
for the Degree of

Master of Science

August 2014

The thesis of Christopher Rumble was reviewed and approved* by the following:

Dennis K. McLaughlin
Professor of Aerospace Engineering
Thesis Co-Advisor

Michael H. Krane
Research Associate and Assistant Professor of Acoustics and Bioengineering
Thesis Co-Advisor

Brent A. Craven
Research Associate and Assistant Professor of Mechanical Engineering
Thesis Co-Advisor

George A. Lesieutre
Professor of Aerospace Engineering
Head of the Department of Aerospace Engineering

*Signatures are on file in the Graduate School

ABSTRACT

The mammalian nose is a multi-purpose organ that houses a convoluted airway labyrinth responsible for respiratory air conditioning, filtering of environmental contaminants, and chemical sensing. Because of the complexity of the nasal cavity, the anatomy and function of these upper airways remain poorly understood in most mammals. However, recent advances in high-resolution medical imaging, computational modeling, and experimental flow measurement techniques are now permitting the study of respiratory airflow and olfactory transport phenomena in anatomically-accurate reconstructions of the nasal cavity. Here, we focus on efforts to fabricate an anatomically-accurate transparent model for planar particle image velocimetry (PIV) measurements. Challenges in the design and fabrication of an optically transparent anatomical model with refractive index-matched working fluid are addressed. PIV velocity field measurements and resistance curve measurements are presented, which will later be used to validate concurrent computational fluid dynamics (CFD) simulations of mammalian nasal airflow.

TABLE OF CONTENTS

List of Figures	vi
List of Tables	viii
List of Symbols	xiii
Acknowledgements	xiii
Chapter 1 Introduction and literature review	1
1.1 Introduction	1
1.2 Literature review	2
1.2.1 The mammalian nasal anatomy	2
1.2.2 Studies of nasal airflow	5
1.2.3 Other experimental studies using optical techniques	5
1.2.2.1 Experimental studies in complex geometries	5
1.3 Objective	6
Chapter 2 Materials and Methods	7
2.1 Experimental Model & Setup	7
2.1.1 Physical Model Design	7
2.1.1.1 Anatomical Reconstruction	8
2.1.1.2 Construction of Refractive Index-Matched Model	13
2.1.1.2 Selection of Refractive Index-Matched Working Fluid	17
2.1.2 Design of Flow Loop	20
2.1.2.1 Scaling Considerations	20
2.1.2.2 Flow Loop	21
2.2 Experimental Measurement	28
2.2.1 Flow Rate Measurement	28
2.2.1.1 Hardware Setup	28
2.2.1.2 Calibration	28
2.2.2 Pressure Measurements	29
2.2.2.1 Hardware Setup	29
2.2.2.2 Calibration	29
2.2.3 PIV Displacement Measurement	30
2.2.3.1 Hardware Setup	31
2.2.3.2 Calibration	33
2.2.4 Data Analysis	34
2.2.4.1 Resistance Curve	34
2.2.4.2 Vector Fields	35
Chapter 3 Results	36

3.1 Cases Studied	36
3.1.1 Inspiratory Flow	36
3.1.1.1 Resistance Curves.....	36
3.1.1.2 PIV Measurements	37
Chapter 4 Summary and Conclusions.....	41
4.1 Summary of Results	41
4.2 Recommendations for Future Work.....	41
Bibliography.....	43
<i>Appendix A</i> Alternative PPIV Data Presentation	48
<i>Appendix B</i> Uncertainty Analysis	59
B.1 Theory.....	59
B.2 Pressure drop	60
B.3 Flow Rate.....	61

LIST OF FIGURES

Figure 1-1. A) An overlay of the eastern gray squirrel nasal geometry. B) A close up of the bilaterally symmetric nasal geometry.	1
Figure 1-2. Cross-sections of various mammalian airways, with the bony structure called turbinates in black and the airway shown in white. Flow is into the page. Complexity is seen to increase from (A) to (D).....	2
Figure 1-3. Sagittal view of the eastern grey squirrel's nasal geometry. a) Naris: entrance of the nasal airway b) dorsal concha c) dorsal meatus d) maxilloturbinal e) maxillary sinus f) naso-palatine canal g) ethmoturbinals h) nasopharynx	3
Figure 1-4. Transverse cross-sections of the nasal geometry of the eastern grey squirrel (life size). a) Naris: entrance of the nasal airway b) dorsal meatus c) dorsal concha d) dorsal meatus e) ventral meatus f) maxilloturbinal g) naso-palatine canal h) nasomaxillary opening i) maxillary sinus j) nasopharynx: exit of the nasal airway k) ethmoturbinals.....	4
Figure 1-5. Distribution of Reynolds number in the nasal airway of the eastern gray squirrel, based on an anatomical reconstruction of the nose and physiological estimates of the flow rate, as in (Craven, et al., 2007).....	5
Figure 2-1. Methodology for generating an anatomically accurate computational and experimental model of the mammalian nasal cavity.....	8
Figure 2-2. Transverse MRI slice in the eastern grey squirrel nasal airway. Blue arrow indicates liquid-filled airways; red arrow points to an air pocket.	9
Figure 2-3. A, raw MRI data slice. B, segmented airway cross-section.	10
Figure 2-4. Three-dimensional surface model of the left nasal airway of the eastern grey squirrel reconstructed from high-resolution MRI data. The red surface is the external nose of the specimen. The grey surface is the internal nasal airway geometry.	11
Figure 2-5. Comparison of rodent nasal anatomy, illustrating the complex nasal airway of the eastern gray squirrel in comparison to other rodent species. Top row shows characteristic nasal airways in the respiratory (maxilloturbinal) region of the nose. Bottom row shows airways located in the olfactory (ethmoturbinal) region (Richter, et al., n.d.).....	12
Figure 2-6. The reconstructed surface model of the left nasal airway of the squirrel (left) was subtracted from a large rectangular block to create a negative of the airway, which was then digitally cut into five sections (right) to simplify fabrication of the experimental model.....	13
Figure 2-7. A view of gridlines is seen through a scaled human nasal cavity model when filled with air (left), water (middle), and an optimal glycerol/water mixture that matches the refractive index of the model (right). (Hopkins, et al., 2000)	14

Figure 2-8. Two sample cubes produced by SLA (left) and PolyJet (right). The SLA layer resolution is 51 microns and the PolyJet layer resolution is 15 microns. The surfaces of the sample parts are unfinished. Nonetheless, note the lack of optical clarity with the PolyJet part.....	14
Figure 2-9. Gridlines can be seen behind a sample SLA cube (2x2x2 in ³). The cube resin is seen scattering light from a 532 nm 100 mw laser beam, which is the same wavelength of light used later in PIV data acquisition.....	15
Figure 2-10. Influence of the alignment of the laser light sheet and camera axis to the layers of an SLA part (Butscher, et al., 2012).....	16
Figure 2-11. Ten times scaled SLA model of the nasal airway of the eastern grey squirrel; nares are at the left; flow is from left to right. Index of refraction of the Somos 11122 resin that was used to fabricate the model is 1.512-1.515 at sodium D-line wavelength.	16
Figure 2-12. Index of refraction of NaI solution as a function of the percent weight of NaI, water, and glycerol. Data points along horizontal lines are the component concentrations of the mixture. Solution was developed with the assistance of J. Taylor of the Penn State Artificial Heart Lab.	18
Figure 2-13. A section of the 10 times scaled physical model immersed in (a) air, (b) water, and (c) optimal index matching NaI solution (55% NaI, 25% glycerol, 20% water by weight) with a grid placed behind the model.	19
Figure 2-14. Planar PIV image acquired inside the physical model filled with NaI solution and seeding particles. The quality of this image and the clarity of the light scattered by the seeding particles demonstrates the potential for acquiring high-quality PIV data in the model.....	19
Figure 2-15. Schematic diagram of the experimental flow loop that was constructed for this study.	22
Figure 2-16. Pressure drop (ΔP) as a function of inspiratory flow rate, Q (ml/min), in the rat nasal airway (from (Schroeter et al, 2012-01)). The curve fits were developed with the equation $\Delta P = a * Q^b$ with the estimated parameters from (Schroeter et al, 2012-01) (Table 2-2).	24
Figure 2-17. Correction factors for viscosity change in centrifugal pumps. To utilize this chart, begin at the pump flow rate (red arrow) and move vertically until an intersection is made with the correct head given by the pump curve. Then, move horizontally left until an intersection is made with the correct viscosity. Continue in a vertical line to find the correction factors (from (Hole, 2014)).....	26
Figure 2-18. AMT ¼-hp centrifugal pump curve for water as the working fluid.	27

Figure 2-19. Operating point of the experimental pumping system for the NaI solution. The operating point can be changed via adjustment of valves. The pump head curve has been corrected for change in viscosity.....	27
Figure 2-21. Planar PIV setup. The camera is perpendicular to the laser light sheet, which is used to illuminate the particle-seeded flow field (from (Ereaut, 2011)).....	31
Figure 2-22. Calculation of the Stokes number in the 10 times scaled model of the squirrel nasal airway for a worst-case air bubble size of 500 μm and a flow rate of 45 L/min.....	33
Figure 2-23. PIV calibration. The same spatial landmarks were identified in the PIV images and the digital 3D model. The in-plane distance between the landmarks was then measured in the 3D model and used as the reference length to calibrate the PIV data.	34
Figure 3-1. Resistance curve for the 10 times scaled model using the NaI refractive index matching fluid the uncertainty bars represent 95% confidence intervals, and were computed using the approach described by (Coleman & Steele, 2009) presented in Appendix B Uncertainty Analysis. Parabola fit of data yielded $\Delta P = 0.0539Q^2 + 0.3214Q - 0.1741$; $R^2 = 0.9991$	37
Figure 3-2. PIV measurement locations. A) Top view of a transparent 3-D rendering of the model with colored lines showing the orientation of the monochromatically colored sagittal planes displayed in B-D, where both the size and location of the PPIV fields of view are shown. ($X_B/W = 0.181$, $X_C/W = 0.0548$, $X_D/W = 0.108$).....	38
Figure 3-3. PPIV velocity vectors at a flow rate of 45 L/min (QHIG H). Red letters indicate the corresponding sagittal plane shown in Figure 3-2. Vectors in every other row and every other column have been omitted for display purposes.	39
Figure 3-4. PPIV velocity vectors at a flow rate of 10 L/min (QLOW). Red letters indicate the corresponding sagittal plane shown in Figure 3-2. Vectors in every other row and every other column have been omitted for display purposes.	40
Figure A-1. PIV velocity vectors in the dorsal meatus at a flow rate of 45 L/min in a sagittal plane located at $X_C/W = 0.0548$ (see Figure 3-2).	48
Figure A-2. PIV velocity vectors in the dorsal meatus at a flow rate of 10 L/min in a sagittal plane located at $X_C/W = 0.0548$ (see Figure 3-2).	49
Figure A-3. PIV velocity vectors in the entrance to the Nasopharynx at a flow rate of 10 L/min in a sagittal plane located at $X_D/W = 0.108$ (see Figure 3-2).	50
Figure A-4. PIV velocity vectors in the entrance to the Nasopharynx at a flow rate of 45 L/min in a sagittal plane located at $X_D/W = 0.108$ (see Figure 3-2).	51
Figure A-5. PIV velocity vectors in the entrance to the Nasopharynx at a flow rate of 45 L/min in a sagittal plane located at $X_D/W = 0.108$ (see Figure 3-2).	52

Figure A-6. PIV velocity vectors in the entrance to the Nasopharynx at a flow rate of 10 L/min in a sagittal plane located at $X_B/W = 0.181$ (see Figure 3-2).	53
Figure A-7. PIV velocity vectors in the entrance to the Nasopharynx at a flow rate of 45 L/min in a sagittal plane located at $X_B/W = 0.181$ (see Figure 3-2).	54
Figure A-8. PIV velocity vectors in the beginning of the Nasopharynx at a flow rate of 10 L/min in a sagittal plane located at $X_B/W = 0.181$ (see Figure 3-2).	55
Figure A-9. PIV velocity vectors in the beginning of the Nasopharynx at a flow rate of 45 L/min in a sagittal plane located at $X_B/W = 0.181$ (see Figure 3-2).	56
Figure A-10. PIV velocity vectors in the end of the Nasopharynx at a flow rate of 10 L/min in a sagittal plane located at $X_D/W = 0.108$ (see Figure 3-2).	57
Figure A-11. PIV velocity vectors in the end of the Nasopharynx at a flow rate of 45 L/min in a sagittal plane located at $X_D/W = 0.108$ (see Figure 3-2).	58

LIST OF TABLES

Table 1-1. Properties of matching fluids. ρ_0 and μ_0 are the density and absolute viscosity of water at 20 °C	6
Table 2-1. Properties of refractive index matching fluids. Percent by weight (w/w)	18
Table 2-2. Estimated parameters for curve fits of pressure drop versus flow rate in the rate nasal passage (from (Schroeter et al, 2012-01)).....	24

LIST OF SYMBOLS

C_L	flow restriction coefficient
d_h	hydraulic diameter
d_p	diameter of seeding particle
f	Darcy skin friction coefficient
g	Gravitational acceleration
K_{eq}	equivalent loss coefficient of the system
K_L	minor loss coefficient or resistance coefficient
K_2	loss coefficients of loop 2
K_3	loss coefficients of loop 3
L	pipe length
l	characteristic length scale of the life size geometry
$L_{laminar}$	settling length required for fully developed laminar pipe flow
Q	volumetric flow rate through model
Q_{LOW}	low volume flow rate (10 L/min)
Q_{HIGH}	high volume flow rate (45 L/min)
Re_{dh}	Reynolds number based on hydraulic diameter of flow passage cross-section
Re_{pipe}	Reynolds number based on pipe diameter
T	the time needed for a fluid particle to transverse an arbitrary distance
TE	time period between the input of the MRI scanner and response (MR signal) of the material.
T_1	Time period for spin-lattice relaxation

T_2	Time period for spin-spin relaxation
U	average velocity of flow
U_o	velocity of free-stream
v	particle's displacement rate
v_s	settling velocity of particle
(w/w)	by weight
α	ratio between characteristic length of the model size and life size
Δd	particle displacement
ΔP	pressure drop across a restriction
ΔP_{Static}	change in static pressure across physical model
Δt	acquisition time between image pairs
ν	kinematic viscosity
ρ	density
ρ_0	density of water at 20 °C
ρ_{air}	density of air
ρ_{NaI}	density of NaI index-matching solution at 20 °C
τ	exponential time constant of the particle velocity
μ_0	absolute viscosity of water at 20 °C
μ_{NaI}	absolute viscosity of NaI index-matching solution at 25 °C

ACKNOWLEDGEMENTS

I first would like to graciously thank my advisors Mike Krane and Brent Craven for giving me this opportunity. My time as a graduate student has allowed me to grow to new understandings. These understandings have laid new philosophies that will help me make a difference in this world. I also would like to thank Dennis McLaughlin for the valuable wisdom he has provided me over my career at Penn State: “work hard, dream big.” Lastly, I thank Josh Taylor for graciously contributing his time to helping me achieve my objective, “I owe you a pint, mate.” This research was supported by the National Science Foundation (grant IOS-1120375).

“second star on the right and on till the morning”

Chapter 1

Introduction and literature review

1.1 Introduction

This thesis will summarize the development of a complex internal flow experiment from specimen to physical model experiments that will be used for validation of computational fluid dynamics (CFD) simulations of mammalian nasal function. The mammals that are being considered in this study are the coyote, deer, bobcat, sea otter, and gray squirrel. Ultimately, the eastern gray squirrel's nasal passage (Figure 1-1) was chosen for the architecture of the scaled benchmark because, under physiological conditions, the squirrel's nasal flow patterns are laminar. Reasoning for laminar flow will be described below. Considerable time was taken in the development of the benchmark under the constraints of data acquisition by means of Planar Particle Image Velocimetry (PIV) techniques.

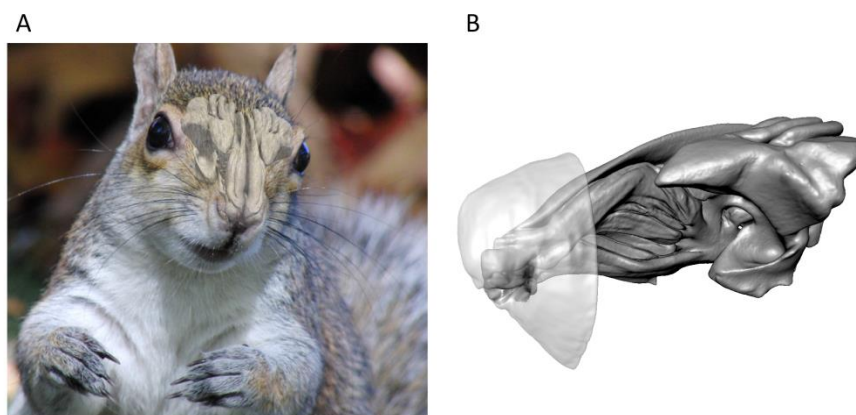


Figure 1-1. A) An overlay of the eastern gray squirrel nasal geometry. B) A close up of the bilaterally symmetric nasal geometry.

1.2 Literature review

1.2.1 The mammalian nasal anatomy

The mammalian nasal airway houses contorted passageways. These passageways are formed by thin bony structures called turbinates (e.g. Figure 1-2). These turbinates, or sometimes called turbinals, are lined with epithelium, which is filled with vasculature and

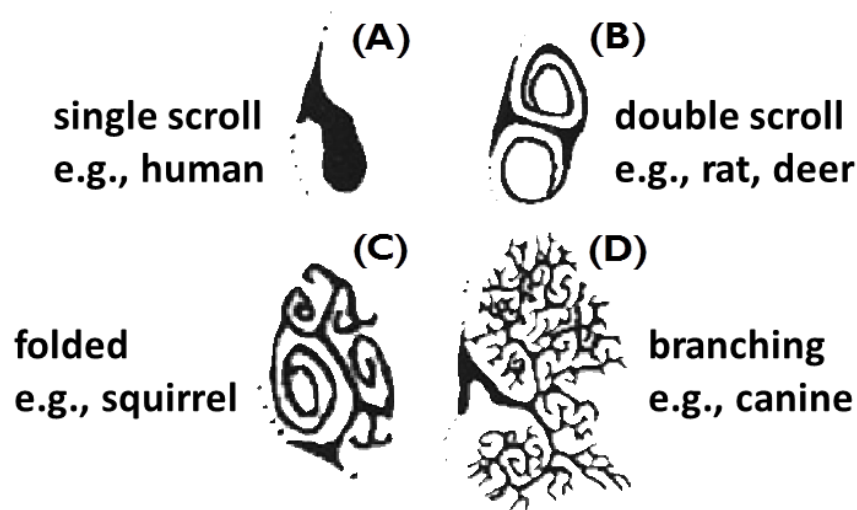


Figure 1-2. Cross-sections of various mammalian airways, with the bony structure called turbinates in black and the airway shown in white. Flow is into the page. Complexity is seen to increase from (A) to (D)

aids in the four primary physiological functions of the mammalian nose: conditioning of inspired air by heat transfer (e.g. heating or cooling), humidification and removing particulates, and sensing odorant molecules.

The nasal cavity is divided into bilaterally-symmetric halves by the nasal septum. The sagittal plane is oriented such that the reflection where the plane intersects is symmetric along the nasal septum. The transverse plane is orthogonal to the sagittal plane. Anatomically, each half of

the nose is comprised of three main regions: the nasal vestibule, the respiratory (maxilloturbinal) region, and the olfactory (ethmoturbinal) region (see Figure 1-3).

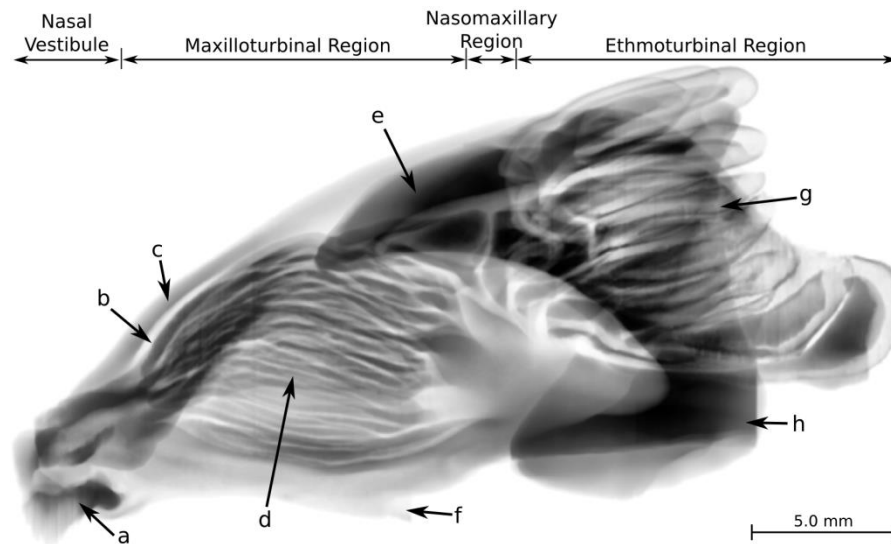


Figure 1-3. Sagittal view of the eastern grey squirrel's nasal geometry. a) Naris: entrance of the nasal airway b) dorsal concha c) dorsal meatus d) maxilloturbinal e) maxillary sinus f) nasopalatine canal g) ethmoturbinals h) nasopharynx

The nasal cavity begins at the naris, into which flow – during inspiration – enters prior to moving caudally into the nasal vestibule. The nasal vestibule is responsible for distributing inspired air to the respiratory and olfactory regions of the nose. Due to the sparse vasculature and small cross-sectional area of the nasal vestibule (see Figure 1-4 for cross-sectional comparison), it is unlikely that the nasal vestibule provides significant heat transfer or “air-conditioning” (Negus, 1958). The nasal vestibule branches into the dorsal meatus and the maxilloturbinal airways. The maxilloturbinal airways, shown in Figure 1-4, is a fractal like branching structure that provides a large surface area for heat

and moisture exchange. Although both are combined with the same organ, the maxilloturbinal air flow (respiratory) is distinctly separate from the ethmoturbinal air flow (olfactory) (Craven, et al., 2010).

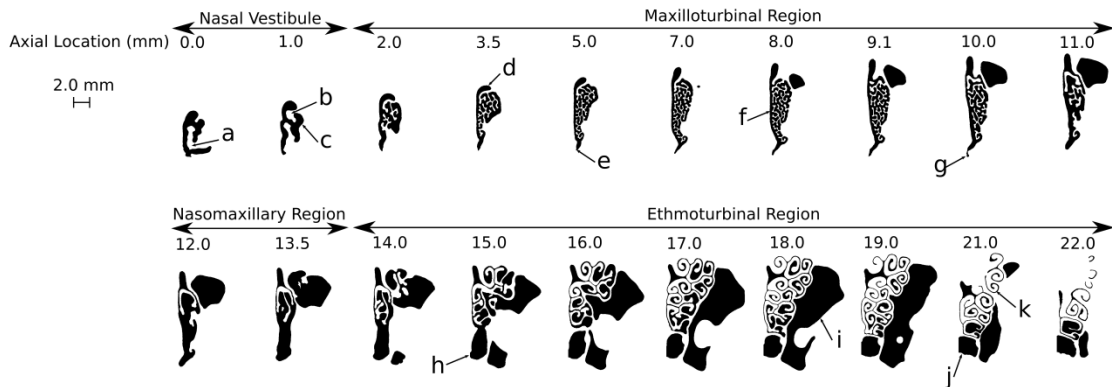


Figure 1-4. Transverse cross-sections of the nasal geometry of the eastern grey squirrel (life size). a) Naris: entrance of the nasal airway b) dorsal meatus c) dorsal concha d) dorsal meatus e) ventral meatus f) maxilloturbinal g) naso-palatine canal h) nasomaxillary opening i) maxillary sinus j) nasopharynx: exit of the nasal airway k) ethmoturbinals.

The primary reason that the squirrel's nasal passageway was chosen is because the flow remains laminar throughout, as demonstrated in Figure 1-5, where the flow is low Reynolds number throughout the squirrel's nasal airway during inspiration at physiological flow rates.

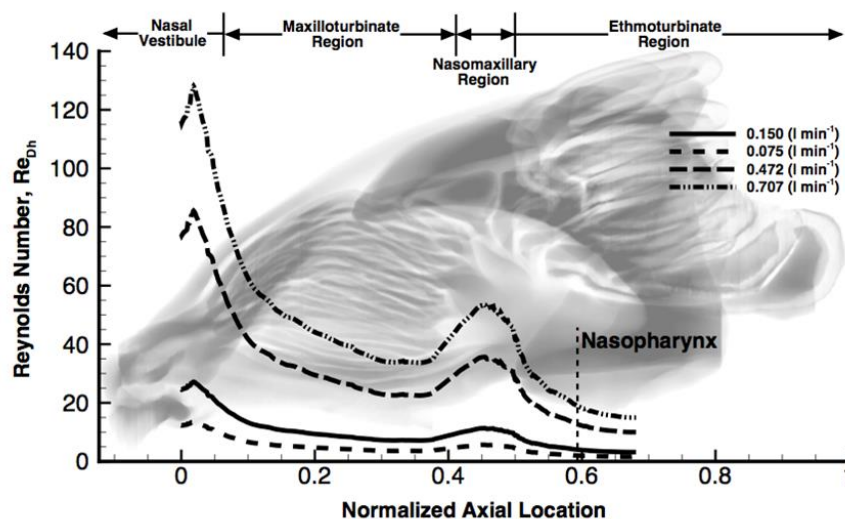


Figure 1-5. Distribution of Reynolds number in the nasal airway of the eastern gray squirrel, based on an anatomical reconstruction of the nose and physiological estimates of the flow rate, as in (Craven, et al., 2007).

1.2.2 Studies of nasal airflow

Previous experimental and computational studies of nasal airflow were extensively summarized by (Lawson, 2010) including experimental studies that utilized rapid prototyping techniques for creating physical models for optical flow measurements using particle image velocimetry. For more information, see section 1.2.3 of (Lawson, 2010).

1.2.3 Other experimental studies using optical techniques

1.2.2.1 Experimental studies in complex geometries

PIV requires that optical distortion of both the light sheet and optical axis of the camera to be minimal to reduce noise in PIV data. To help reduce these optical distortions, index matching of the working fluid and an optically clear model are employed. In Table 1-1, provided by (Budwig, 1994), are a list of properties of aqueous solutions and organic liquids that have been used in various experiments where the working fluid was indexed matched with the experimental model.

Table 1-1. Properties of matching fluids. ρ_0 and μ_0 are the density and absolute viscosity of water at 20 °C

	n	ρ/ρ_0	μ/μ_0	References and comments
Aqueous solutions				
glycerin	1.33–1.47	1–1.26	1–1490	
zinc iodide	1.33–1.62			Hendricks and Avram (1981), range of v/v_0 is 1 to 10
sodium iodide	1.5 60% NaI by wt.			Chen and Fan (1992)
potassium thiocyanate	1.33–1.49	1–1.39	1–2.4	Jan et al. (1989), mix with glycerin to increase viscosity
ammonium thiocyanate	1.33–1.50	1–1.15	1–2.1	Hooper (1992)
sodium thiocyanate	1.33–1.48	1–1.34	1–7.5	Duncan et al. (1990)
Organic liquids				
kerosene	1.45	0.82		Bovendeerd et al. (1987)
silicone oil mixture	1.47	1.03	190	Edwards and Dybbs (1984)
mineral oil (paraffin oil)	1.48	0.85		
turpentine	1.47	0.87	1.49	
solvent naphtha	1.50	0.67		
soybean oil	1.47	0.93	69	
olive oil	1.47	0.92	84	
castor oil	1.48	0.96	986	
tung oil	1.52	0.93		
cassia oil	1.60			Sinkankas (1966)
dibutylphthalate	1.49			Hendricks and Avram (1981): caution, expiratorogen
Mixture of oil of turpentine and tetrahydronaphthalene (Tetraline)		~ 1	~ 1	Liu et al. (1990)

The solution containing zinc iodide demonstrated a wide range of index matching and according to (Hendriks & Aviram, 1982) the solution also has electrochromic properties. Placing an electrified anode in the free stream will produce a dark brown trace of iodide. This property could be used for flow visualization. The iodide trace can be reversed by adding a reducing agent.

1.3 Objective

The objective of this research is to create an anatomically accurate experimental model of a complex rodent nasal airway and to acquire PIV measurements in the model for validation of concurrent CFD simulations. The results of this work are intended to contribute to the fundamental understanding of nasal form and function in mammals, and to advance current state-of-the-art optical flow measurement techniques in complex experimental models.

Chapter 2

Materials and Methods

2.1 Experimental Model & Setup

In this chapter the design of both the experimental setup and the experimental model will be presented. Scaling methods were applied in the development of the experimental model to maintain dynamic similarity with physiological conditions. Methods for calibrating PIV measurements in a complex internal flow geometry will also be presented.

2.1.1 Physical Model Design

The internal architecture of the physical model was created through a five step process, (Figure 2-1). Given the aim to acquire experimental data via optical techniques, constraints associated with these techniques were considered during the development of the model.

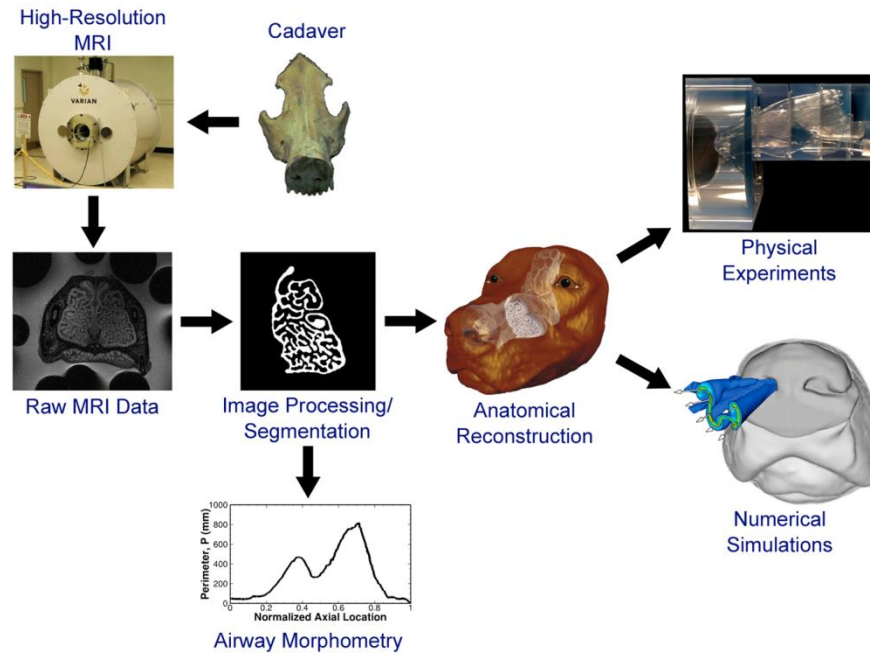


Figure 2-1. Methodology for generating an anatomically accurate computational and experimental model of the mammalian nasal cavity.

2.1.1.1 Anatomical Reconstruction

A female eastern grey squirrel (*Sciurus carolinensis*) specimen with a mass of approximately 418 g was acquired in central Pennsylvania (PA) from a local hunter in accordance with the regulations of the PA Game Commission. The head was removed and preserved in 4% paraformaldehyde solution. High-resolution magnetic resonance imaging (MRI) scans were acquired, which resolve the bone and epithelium in the nasal passageway (De Rycke, et al., 2003). A MRI contrast agent, Magnevist (Bayer, Germany), was used to improve the quality of the MRI scans.

Acquisition of MRI data consists primarily of time periods: T_1 , T_2 and TE. T_1 and T_2 are associated with the magnetic response of the material in question. TE is the time period between the input of the MRI scanner and measurement of the response (MR signal) of the material. The

response is dependent on proton density of the tissues (Weishaupt, et al., 2003). In order to collect accurate anatomical information, the nasal cavity needs to be completely filled with liquid, as pockets of air can distort the surrounding tissue and corrupt the MRI scans (see Figure 2-2.)

The removal of trapped air required the specimen to be submerged in solution. The specimen was oriented in various positions such that air bubbles were seen exiting at the nares and at the nasopharynx. In some anatomically complex regions, a vacuum pump had to be used to help dislodge more entrained air pockets located in the internal nasal geometry. The submerged specimen was sealed into a latex sheath with zip ties. The sealed specimen was then placed into the 14-Tesla MRI scanner (Agilent Technologies, USA). High-resolution MRI scans were then acquired with an isotropic resolution of 40 microns.

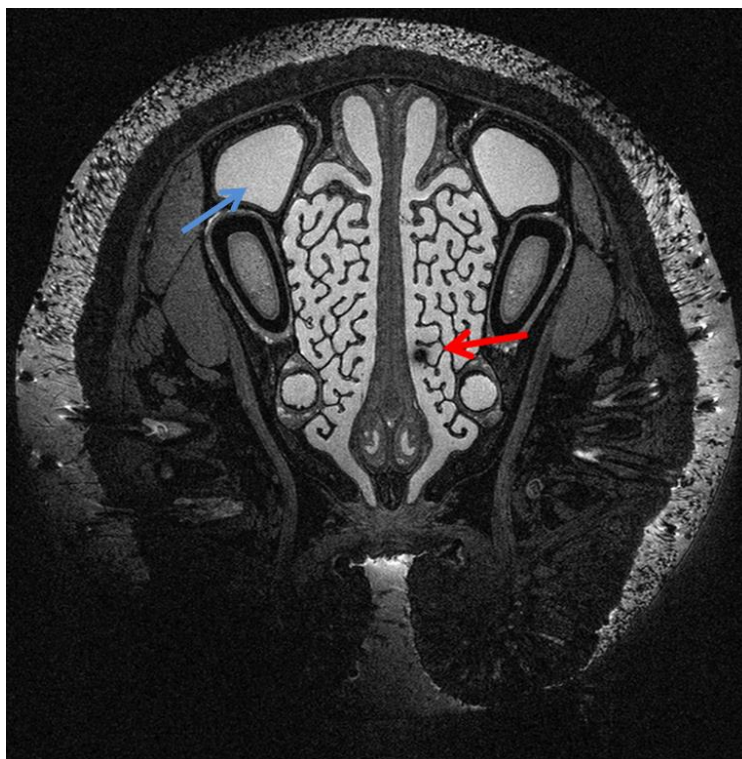


Figure 2-2. Transverse MRI slice in the eastern grey squirrel nasal airway. Blue arrow indicates liquid-filled airways; red arrow points to an air pocket.

Image segmentation of the left nasal airway (Figure 2-3) was accomplished using Avizo (Visualization Sciences Group, USA). Due to preliminary image processing, segmentation of large airways was trivial and was mostly accomplished by means of algorithmic schemes available in Avizo including region growing, thresholding, contour extraction by means of edge detection, and contour interpolation and extrapolation in the axial direction.

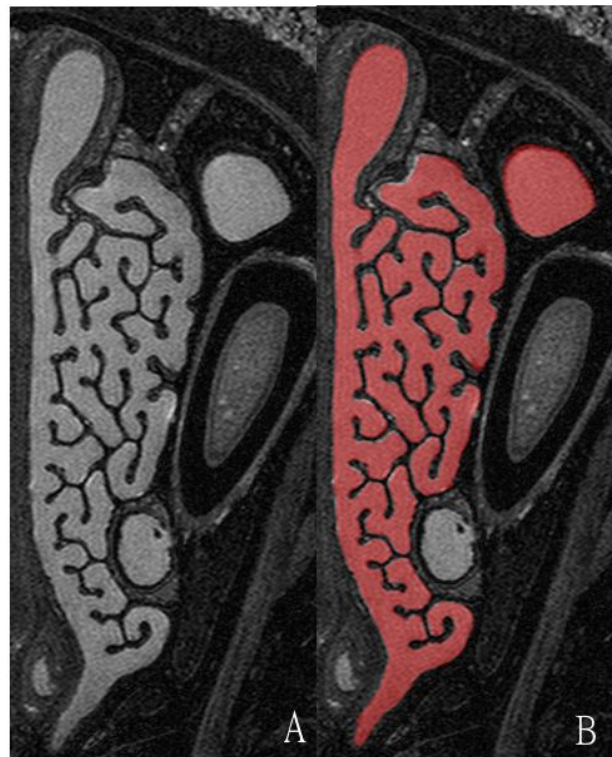


Figure 2-3. A, raw MRI data slice. B, segmented airway cross-section.

After segmenting the MRI data, a three-dimensional surface model was then generated by means of a modified form of the marching cubes algorithm (Lorensen & Cline, 1987) available in Avizo, yielding a triangulated surface mesh of the nasal airway. Slight subsequent surface smoothing was then performed to reduce surface castellation or “staircasing” (Taubin, 1995), yielding the final reconstructed surface model of the left nasal airway (Figure 2-4).

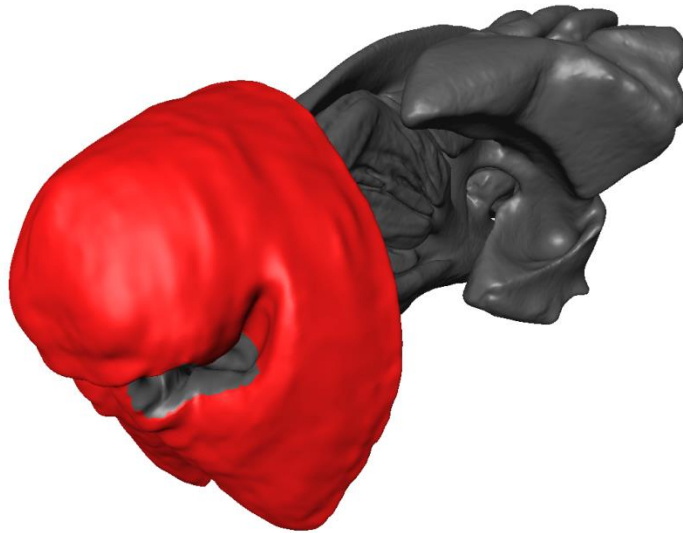


Figure 2-4. Three-dimensional surface model of the left nasal airway of the eastern grey squirrel reconstructed from high-resolution MRI data. The red surface is the external nose of the specimen. The grey surface is the internal nasal airway geometry.

Experimental study of flow in the nasal airway of keen-scented mammals has proven challenging. To advance state-of-the-art optical flow measurement techniques in complex anatomical models, one of the reasons that we chose the eastern gray squirrel is due to its more complex nasal anatomy compared with most other rodent species, as illustrated in Figure 2-5, while being less complex than other keen-scented species, such as the canine (Craven et al., 2007). However, the nasal airways of the gray squirrel have characteristic dimensions on the order of 1 mm, making it difficult to study flow patterns in detail at 1:1 scale. Thus, we chose to fabricate a 10 times life size physical model for optical flow measurements.

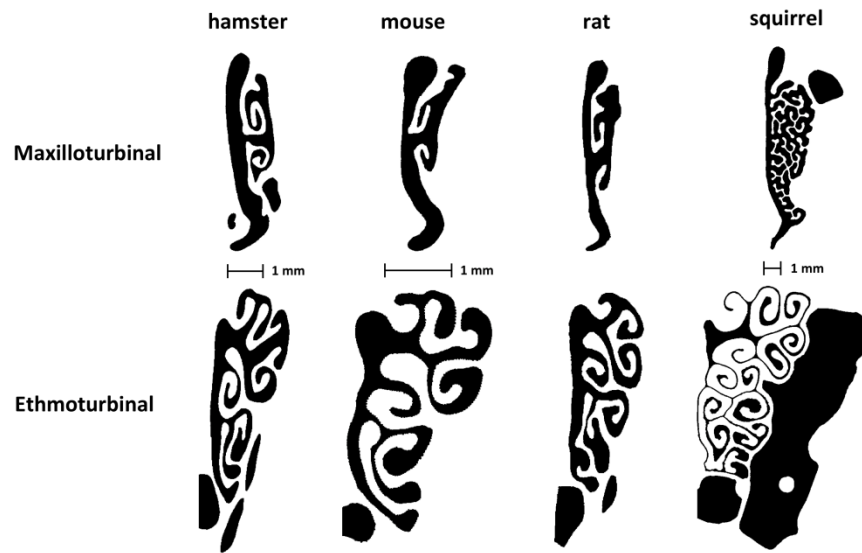


Figure 2-5. Comparison of rodent nasal anatomy, illustrating the complex nasal airway of the eastern gray squirrel in comparison to other rodent species. Top row shows characteristic nasal airways in the respiratory (maxilloturbinal) region of the nose. Bottom row shows airways located in the olfactory (ethmoturbinal) region (Richter, et al., n.d.).

To generate a digital stereolithography (SLT) file for fabrication, the reconstructed surface model was prepared in the commercial software package Magics (Materialise, USA). In particular, the model was first scaled by 10 times life size. Then, Boolean operations were used to subtract the 3-D surface geometry from a large rectangular volume, to yield a “negative” of the airway. The airway negative was then digitally cut into five sections (Figure 2-6) to simplify the fabrication of the physical model.

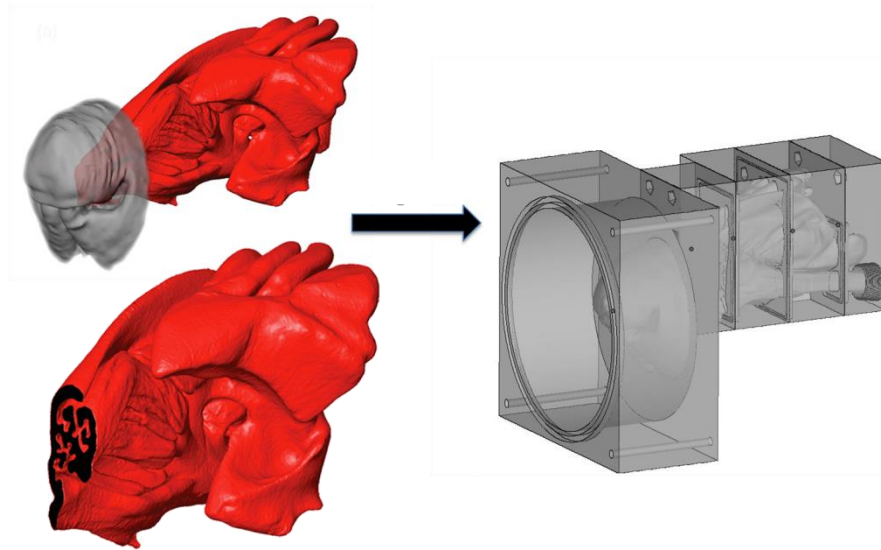


Figure 2-6. The reconstructed surface model of the left nasal airway of the squirrel (left) was subtracted from a large rectangular block to create a negative of the airway, which was then digitally cut into five sections (right) to simplify fabrication of the experimental model.

2.1.1.2 Construction of Refractive Index-Matched Model

An ideal index matched experiment should consist of an optically clear model that shares the same index of refraction with a colourless working fluid.

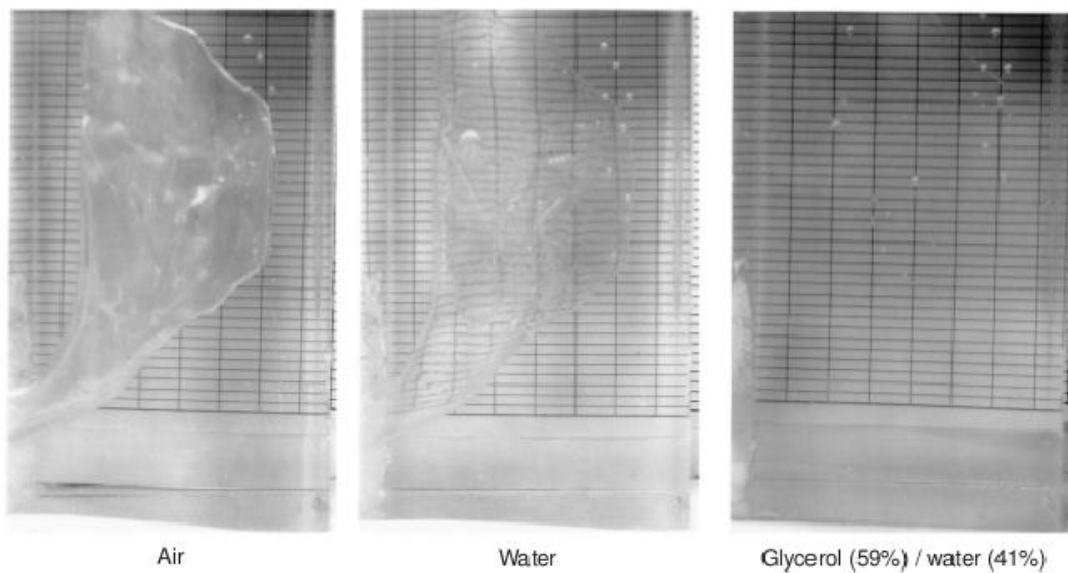


Figure 2-7. A view of gridlines is seen through a scaled human nasal cavity model when filled with air (left), water (middle), and an optimal glycerol/water mixture that matches the refractive index of the model (right). (Hopkins, et al., 2000)

Of the rapid prototyping techniques available in industry two were chosen as candidate techniques for fabricating the nasal airway model: PolyJet & stereolithography (SLA). SLA is an additive fabrication process; it constructs the object in a vat of UV-curable photopolymer via a computer-controlled laser. PolyJet uses inkjet heads to displace UV-curable material onto a build tray. The photopolymer material is cured upon exit of the inkjet by laser light. Both processes produce the 3-D object layer by layer. After careful examination of samples created using both techniques, the SLA technique was chosen for its optical clarity, as seen in Figure 2-8.

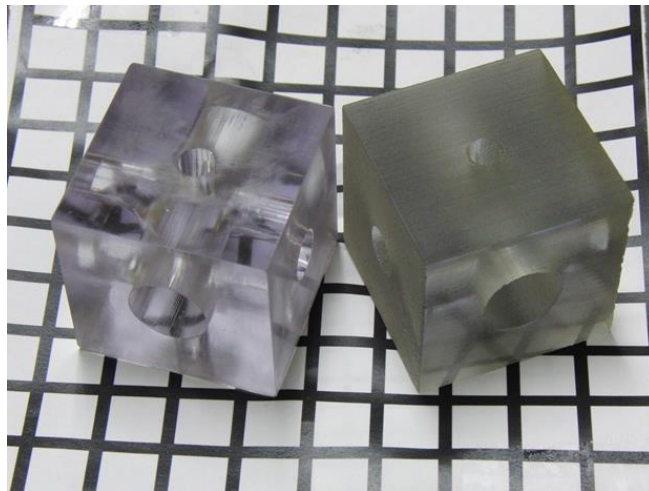


Figure 2-8. Two sample cubes produced by SLA (left) and PolyJet (right). The SLA layer resolution is 51 microns and the PolyJet layer resolution is 15 microns. The surfaces of the sample parts are unfinished. Nonetheless, note the lack of optical clarity with the PolyJet part.

It is important to note that, in our experience, SLA did not produce a perfect, optically transparent part. Due to slight optical inhomogeneity in the material, sample SLA parts were somewhat opaque (Figure 2-8), resulting in the part scattering light (Figure 2-9), which is undesirable for PIV measurements. To minimize this effect, the amount of SLA material was

minimized by keeping the viewing walls as thin as structurally possible to minimize light scattering.

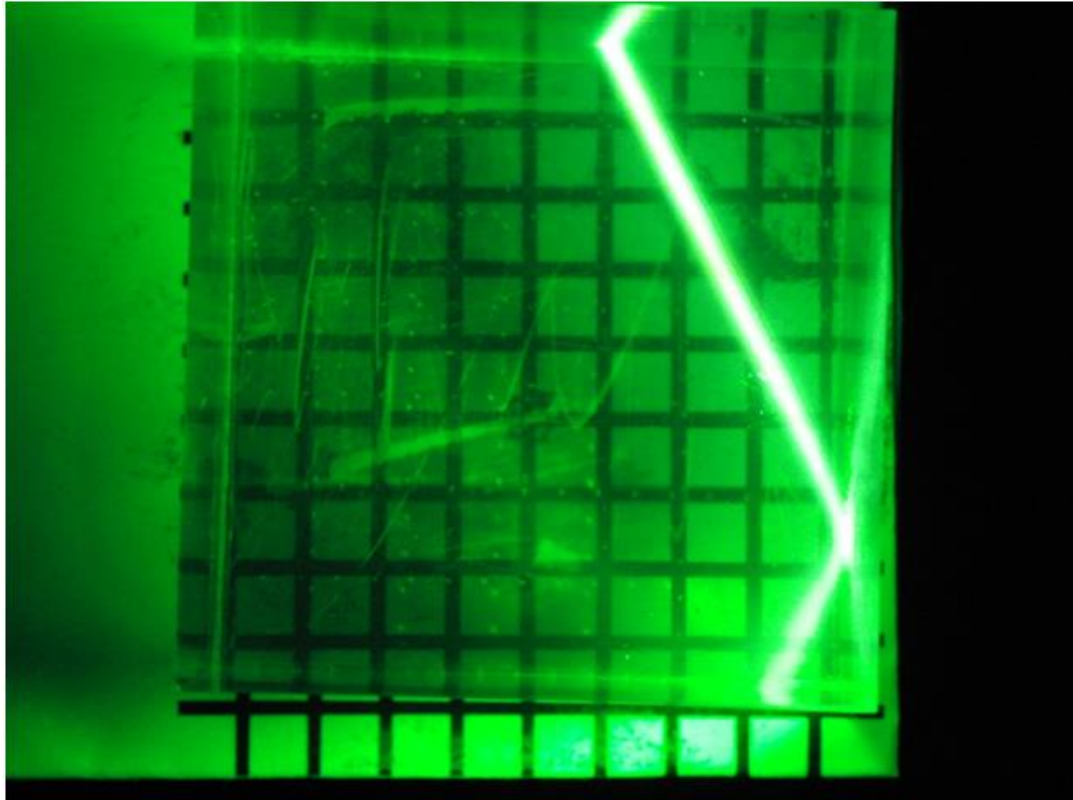


Figure 2-9. Gridlines can be seen behind a sample SLA cube (2x2x2 in³). The cube resin is seen scattering light from a 532 nm 100 mw laser beam, which is the same wavelength of light used later in PIV data acquisition.

Lastly, it is important to note the significance of the orientation of the PIV instrumentation (i.e., camera and light sheet). In particular, due to optical inhomogeneity in the material caused by the SLA layering, light rays that are parallel to the plane of the layering are distorted. This effect can be minimized by orienting the PIV light sheet and camera at 45° angles to the layering of the SLA part (see Figure 2-10 for illustration). Accordingly, the 10 times scaled nasal airway model was fabricated with these constraints via the SLA process by Forecast3D (Carlsbad, CA), Figure 2-11.

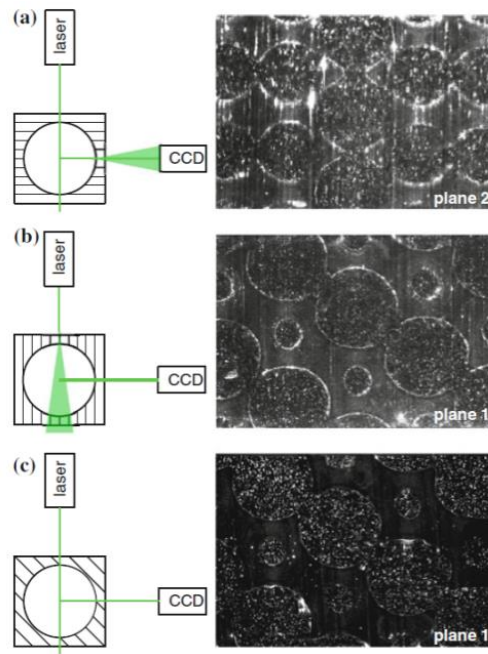


Figure 2-10. Influence of the alignment of the laser light sheet and camera axis to the layers of an SLA part (Butscher, et al., 2012).

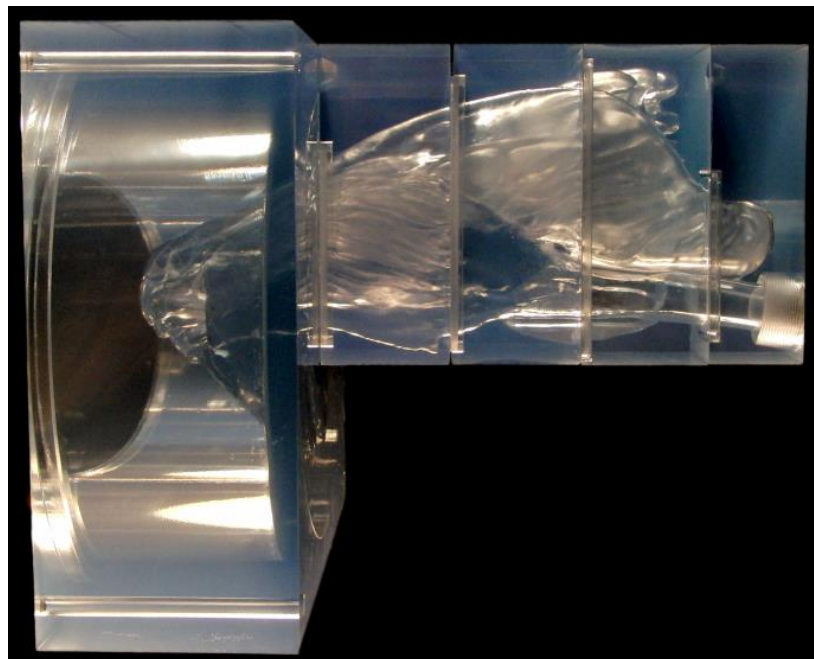


Figure 2-11. Ten times scaled SLA model of the nasal airway of the eastern grey squirrel; nares are at the left; flow is from left to right. Index of refraction of the Somos 11122 resin that was used to fabricate the model is 1.512-1.515 at sodium D-line wavelength.

2.1.1.2 Selection of Refractive Index-Matched Working Fluid

The task of locating a viable fluid for index matching proved to be very difficult. The ideal criteria for such a fluid include: low toxicity, nonflammable, low volatility, non-corrosive, colourless in appearance and cost effective (Hendriks & Aviram, 1982). The three potential index-matching solutions that were considered – out of numerous toxic and expensive fluids – are: NaI solution (sodium iodide, glycerol, water mixture), anisole, and a clove and safflower oil mixture (see Table 2-1 for properties).

In preliminary experiments the clove and safflower oil solution demonstrated problems with a cloudy suspension when contaminated with water; though, this cloudy suspension was shown to be reversible over time. Anisole was viable due its cheapness, but its flammability and high volatility make it dangerous to work with in large quantities. The NaI solution is corrosive to metal and the solution can obtain a yellow discoloration, which is caused by the formation of I_3^- ions; however, the discoloration can be prevented or reversed with the addition of 0.1 percent (by weight) sodium thiosulfate to the solution (Narrow et al, 2000-03).

Accordingly, NaI solution was chosen as the working fluid because it is safe to work with, relatively inexpensive, and it is possible to produce a range of refractive indices by varying the relative concentration of sodium iodide, glycerol, and water (Figure 2-12). A NaI solution was produced to match the refractive index of the physical model (1.512-1.515) using 55% NaI, 25% glycerol, and 20% water (by weight). Optical experiments were then performed to ensure that the index of refraction between the working fluid and the physical model were indeed the same (Figure 2-13 and Figure 2-14).

Table 2-1. Properties of refractive index matching fluids. Percent by weight (w/w)

	density (g/ml)	kinematic viscosity (cSt)	index of refraction
Anisole	0.989	1.06 @25 °C	1.516*
Clove:Safflower 4:1 by volume	0.9704	12.5 @25 °C	1.5135-1.5150*
NaI(55%) Glycerol (25%) Water (20%) (w/w)	1.847	13.4 @25 °C	1.519-1.516*
* Sodium D line			

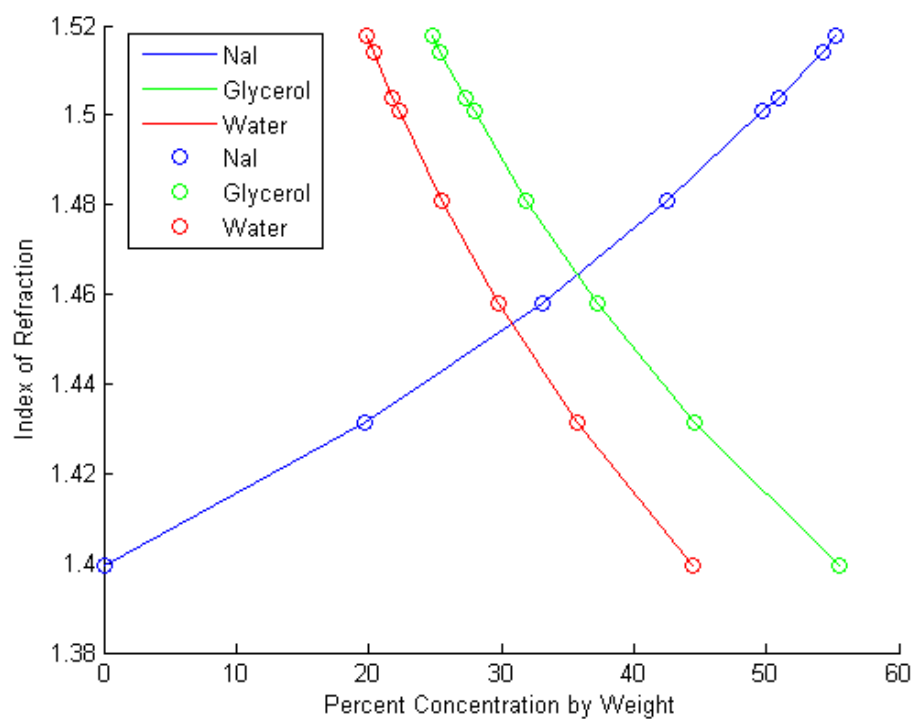


Figure 2-12. Index of refraction of NaI solution as a function of the percent weight of NaI, water, and glycerol. Data points along horizontal lines are the component concentrations of the mixture. Solution was developed with the assistance of J. Taylor of the Penn State Artificial Heart Lab.

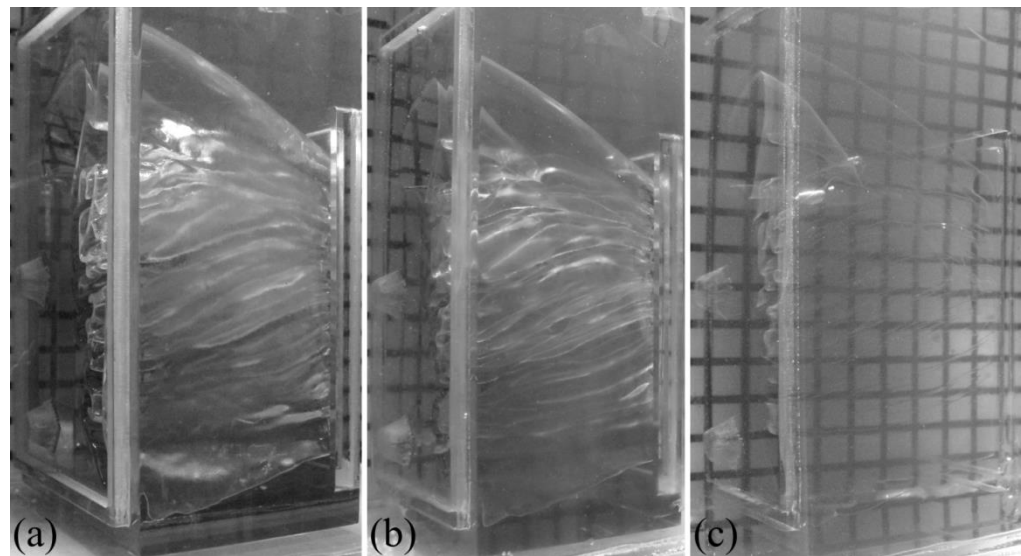


Figure 2-13. A section of the 10 times scaled physical model immersed in (a) air, (b) water, and (c) optimal index matching NaI solution (55% NaI, 25% glycerol, 20% water by weight) with a grid placed behind the model.

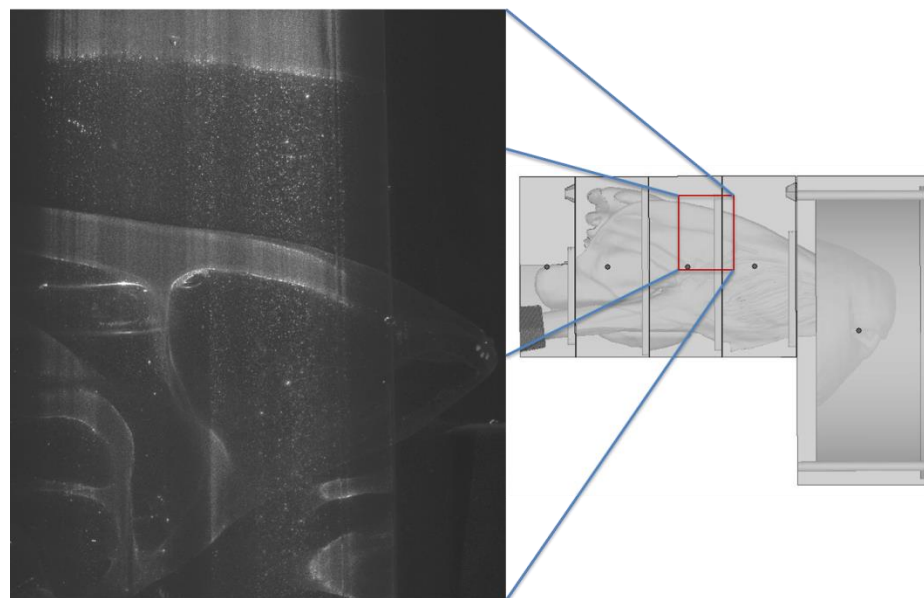


Figure 2-14. Planar PIV image acquired inside the physical model filled with NaI solution and seeding particles. The quality of this image and the clarity of the light scattered by the seeding particles demonstrates the potential for acquiring high-quality PIV data in the model.

2.1.2 Design of Flow Loop

2.1.2.1 Scaling Considerations

Scaling relationships between the life size specimen and the scaled physical experimental model will be presented for the following parameters: flow rates, pressure drop, and time scale.

To maintain dynamic similarity between life size and scaled models, the Reynolds between the two must be equal. Accordingly, Reynolds similarity dictates that

$$\frac{Q_m}{Q_l} = \alpha \frac{\nu_m}{\nu_l} \quad (2.1)$$

where Q is the volumetric flow rate, α is the ratio between model size and life size, and ν is kinematic viscosity. The subscripts l represents the life size geometry of the airway and m represents the scaled experimental model. The volumetric flow rate Q is

$$Q = A * U \quad (2.2)$$

where U is the average velocity that is normal to the cross-sectional area A . Similarity in Womersley number of life size and scaled model will require that

$$\frac{T_m}{T_l} = \alpha^2 * \frac{\nu_m}{\nu_l} \quad (2.3)$$

with T representing the time needed for a fluid particle to transverse an arbitrary distance.

Considering the nasal airway as an internal flow restriction, equation (2.4) may be used for scaling of static pressure drop:

$$\Delta P = C_L \rho U^2 \quad (2.4)$$

where ρ is the density of the working fluid and ΔP is the change in pressure across the restriction. Flow losses across such a restriction are a function of the coefficient C_L , which is independent of scale when Reynolds number is matched. Combining equations (2.1) , (2.2) and (2.4) yields

$$\frac{\Delta P_m}{\Delta P_l} = \frac{\rho_m}{\rho_l} \frac{v_m^2}{v_l^2} \frac{1}{\alpha^2} \quad (2.5)$$

where $\frac{\Delta P_m}{\Delta P_l}$ represents the static pressure drop ratio between model scale and the life size models of the nasal cavity.

2.1.2.2 Flow Loop

All of the design consideration of the experimental flow loop will be described in this section.

For the flow entering the diffuser to be fully developed, the minimum distance required to achieve fully-developed laminar flow is given by

$$L_{laminar} = 0.05 * D_{pipe} * Re_{pipe} \quad (2.6)$$

where D_{pipe} and Re_{pipe} are the pipe diameter and Reynolds number, respectively.

Pump selection required that the pressure drop caused by both the major and minor losses of the system be accounted for via

$$\Delta P = f * \frac{L}{D_{pipe}} * \frac{\rho}{2} * U^2 + \Sigma K_L * \frac{\rho}{2} * U^2 \quad (2.7)$$

where

$$f = \frac{64}{Re} \quad (2.8)$$

and L is the pipe length and K_L is the minor loss coefficient or resistance coefficient.

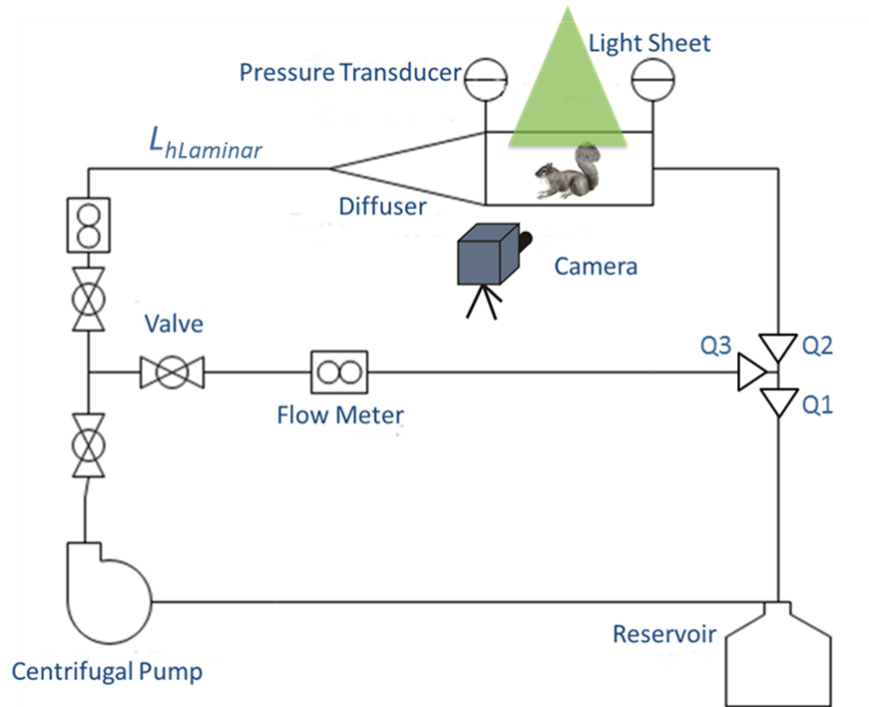


Figure 2-15. Schematic diagram of the experimental flow loop that was constructed for this study.

As seen in Figure 2-15, a secondary loop was implemented to allow flow to bypass the experimental model. This bypass method was utilized to control the flow through the experiment while allowing the pump to operate near its best efficiency point.

A relationship was derived to better understand how the system responds to flow rate control. The pressure drop across a closed loop is equal to the summation of flow losses across that loop, i.e.

$$\Delta P = \Sigma K Q^2 \quad (2.9)$$

$$Q_1 = Q_2 + Q_3 \quad (2.10)$$

with Equation (2.10) being the nodal flow rate relationship that is depicted in the lower right flow loop junction in Figure 2-15. The bypass loop and the experimental loop are in parallel. Thus, it was assumed that flow rates through these branches experience the same pressure drop. Now, combining equation (2.9) and (2.10) leads to the following

$$\sqrt{\frac{\Delta P}{K_{eq}}} = \sqrt{\frac{\Delta P}{K_2}} + \sqrt{\frac{\Delta P}{K_3}} \quad (2.11)$$

which simplifies to

$$K_{eq} = \frac{K_2}{\left(1 + \frac{\sqrt{K_2}}{\sqrt{K_3}}\right)^2} \quad (2.12)$$

K_{eq} is the equivalent loss coefficients of the system influenced by the pump, and K_2 & K_3 represent the loss coefficients of each loop.

The maximum inspiratory flow rate through and pressure drop across the squirrel nasal passage was approximated from data on a Sprague-Dawley rat provided by (Schroeter et al, 2012-01) (Figure 2-16; Table 2-2).

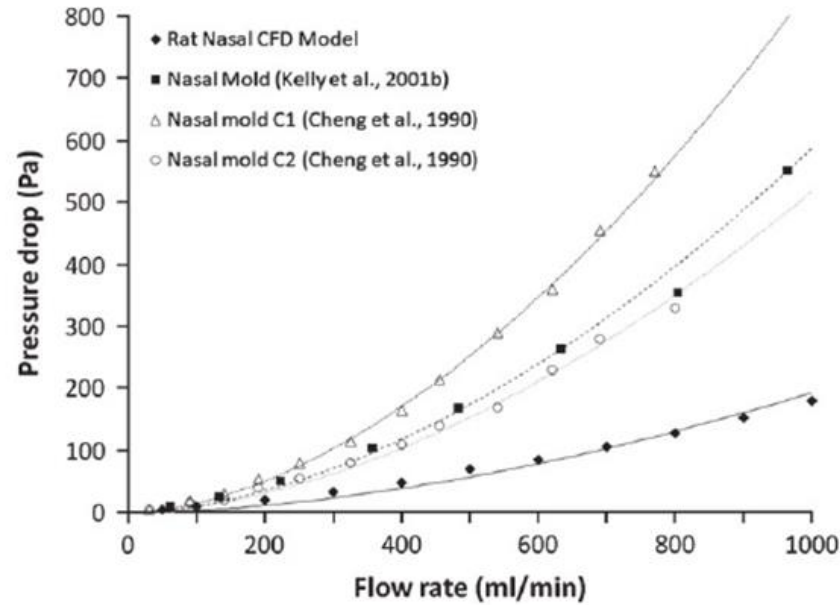


Figure 2-16. Pressure drop (ΔP) as a function of inspiratory flow rate, Q (ml/min), in the rat nasal airway (from (Schroeter et al, 2012-01)). The curve fits were developed with the equation $\Delta P = a * Q^b$ with the estimated parameters from (Schroeter et al, 2012-01) (Table 2-2).

Table 2-2. Estimated parameters for curve fits of pressure drop versus flow rate in the rate nasal passage (from (Schroeter et al, 2012-01))

Estimated parameters for the pressure-flow curves of the form $\Delta p = aQ^b$, Δp (Pa), Q (m³/s).

Nasal replica cast/CFD model	<i>a</i>	<i>b</i>	<i>R</i> ²
CFD model	0.025×10^7	1.75	0.9951
Nasal replica cast (Kelly et al., 2001b)	0.076×10^7	1.75	0.9936
Nasal replica cast C1 (Cheng et al., 1990)	0.110×10^7	1.75	0.9988
Nasal replica cast C2 (Cheng et al., 1990)	0.067×10^7	1.75	0.9957

The Sprague-Dawley flow rate data was used as an estimate for the experimental setup since the eastern gray squirrel is of similar size to the rat. Though physiologically flow rates are likely to be similar, the added complexity of the squirrel's nasal passage likely results in higher flow losses (i.e., pressure drop). Thus, these life size flow rates

were used with equation (2.1) to estimate the flow rate conditions at model scale in the present study.

Analysis of pump performance was carried out to properly size the pump for the experiment. A quarter horsepower centrifugal pump (Figure 2-18) was chosen with a high rpm to minimize flow pulsation. It was also necessary to correct for the effects of higher viscosity of the working fluid, as available pump curves are only rated for pumping water.

In general, an increase in viscosity will increase brake horsepower requirement and cause a reduction in head, capacity, and efficiency of the pump. It is thus necessary to establish

$$Q_{new} = C_Q * Q_{old} \quad (2.13)$$

and

$$h_{new} = C_h * h_{old} \quad (2.14)$$

where C_h and C_Q are correction factors for viscosity change derived from Figure 2-17. Figure 2-18 shows the unadulterated pump curve and Figure 2-19 the corrected pump curve for as well as an operating point of the experimental flow loop.

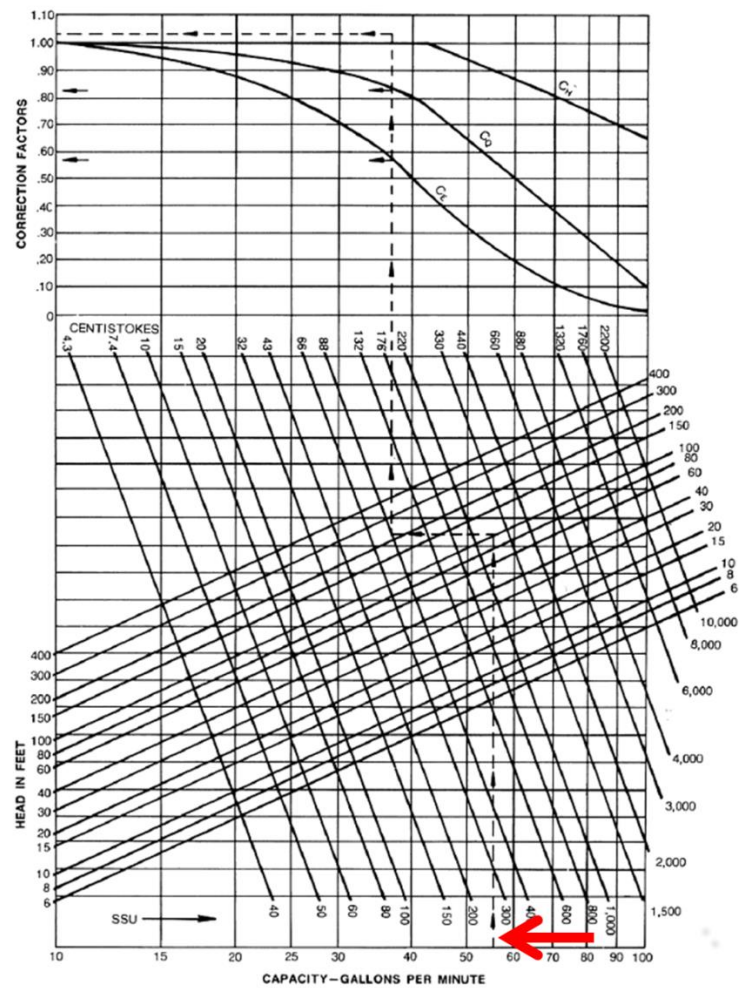


Figure 2-17. Correction factors for viscosity change in centrifugal pumps. To utilize this chart, begin at the pump flow rate (red arrow) and move vertically until an intersection is made with the correct head given by the pump curve. Then, move horizontally left until an intersection is made with the correct viscosity. Continue in a vertical line to find the correction factors (from (Hole, 2014)).

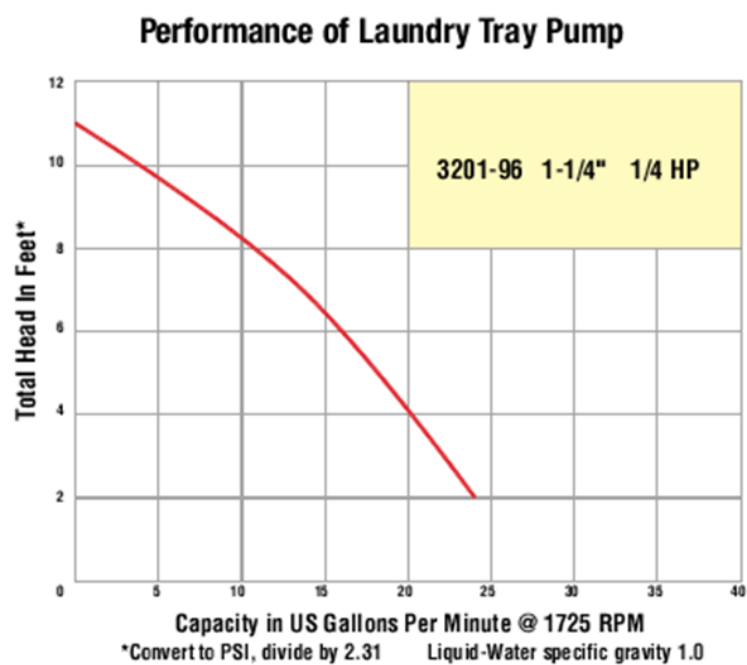


Figure 2-18. AMT 1/4-hp centrifugal pump curve for water as the working fluid.

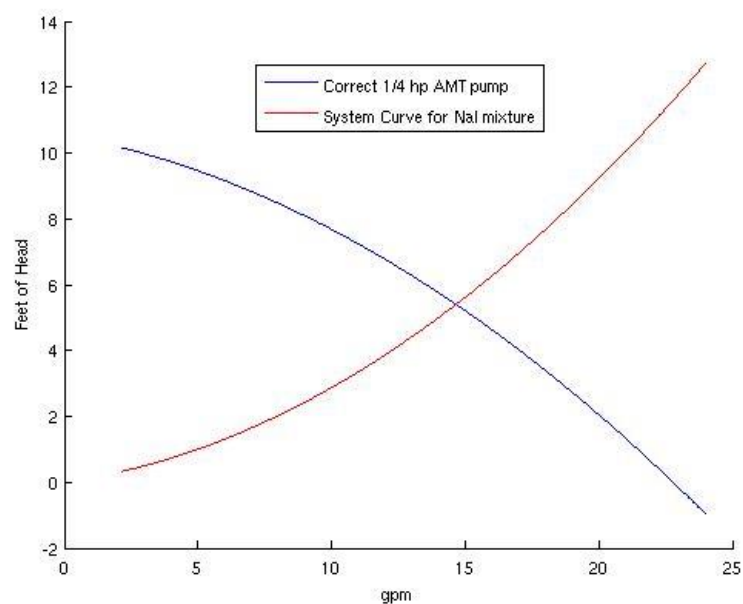


Figure 2-19. Operating point of the experimental pumping system for the NaI solution. The operating point can be changed via adjustment of valves. The pump head curve has been corrected for change in viscosity.

2.2 Experimental Measurement

This section will provide an overview of hardware used during the experiment, calibration methods, and post-processing and data reduction techniques.

2.2.1 Flow Rate Measurement

2.2.1.1 Hardware Setup

The flow rate was measured using an ultrasonic flow meter (Transonic, USA). The flow rate measurement was shown to be insensitive to the mounting orientation of the flow meter. This type of flow meter is non-restrictive, as it uses acoustic waves to measure the flow rate. The flow meter was placed in line with the experiment.

2.2.1.2 Calibration

Transonic Systems Inc. certifies that the flow meter was calibrated according to NIST (National Institute of Standards and Technology) standards and to the Transonic System Inc. equipment performance standards. Maximum unadjusted zero flow error of the Transonic flow meter is +/- 300ml/min. The maximum error in the absolute volume flow rate is +/- 10 % of reading plus the zero flow error.

2.2.2 Pressure Measurements

2.2.2.1 Hardware Setup

Pressure ports were located just forward of the nose and aft of the nasopharynx (see Figure 2-15). The pressure port forward of the nose was located just downstream of the exit of the diffuser. It is important to note that the pressure port forward of the nose also served as a venting port to allow gas to escape during the filling and the draining processes of the system. The pressure transducers were connected to their respective ports: pressure transducer 1 was attached to the forward port and pressure transducer 2 was attached to the aft port. The pressure transducers themselves were placed at the same height.

2.2.2.2 Calibration

Calibration of each transducer was performed with the use of a monometer. An amplifier was employed to amplify the DC voltage output of the transducer. A multi-meter was used to read the output of the transducer. Voltage readings were recorded with varying fluid heights and the fluid heights were then converted to pressures via the hydrostatic relationship, resulting in a calibration curve for each transducer (Figure 2-20).

NaI index matching solution was used as the working fluid for pressure transducer calibration. A plumb bob was used to reduce error in fluid column height measurement. Pressure transducers were manufactured by Argon Medical Transducer (USA): reference number 041516504A.

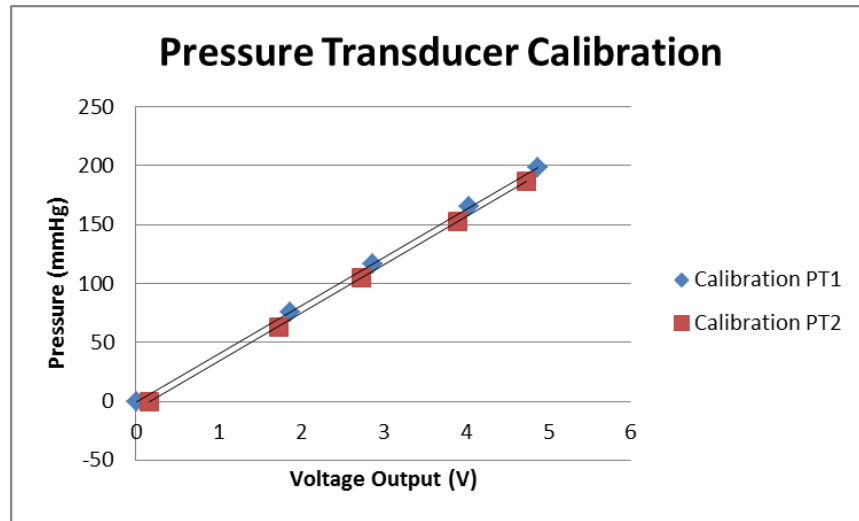


Figure 2-20. Calibration for pressure transducers 1 & 2. (PT1 $P=41.919V+0.685$ $R^2 = 0.9997$)
(PT2 $P=43.059V-4.0367$ $R^2=0.9986$)

2.2.3 PIV Displacement Measurement

The non-intrusive optical measurement technique that was used in this thesis was particle image velocimetry (PIV). With roots originating from laser Doppler velocimetry (LDV) and laser speckle velocimetry, PIV is rapidly becoming the primary optical technique used today.

For background, PIV uses a pulsed laser light sheet to illuminate “seed particles” that are injected into the flow (see Figure 2-22). These particles scatter light, which is detected by a digital camera. Image acquisition is synchronized with the pulsing of the light sheet. Each cycle has two laser pulses synced with two image exposers. These images, or an image pair, are then processed to obtain a displacement field of the seed particles, which is used to calculate velocity via the following relationship and the known time difference between the acquired images

$$v = \Delta d / \Delta t \quad (2.15)$$

where v is the velocity vector, Δd is the average particle displacement in each interrogation region in the image, and Δt is the time delay between laser pulses.

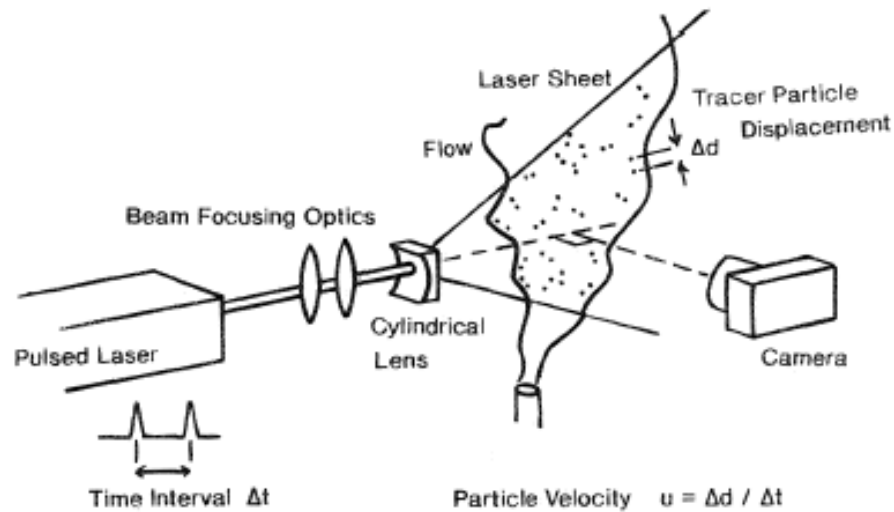


Figure 2-21. Planar PIV setup. The camera is perpendicular to the laser light sheet, which is used to illuminate the particle-seeded flow field (from (Ereaut, 2011)).

2.2.3.1 Hardware Setup

A crucial step is to align the following objects in the correct manner: light sheet, layer orientation of the rapid prototyped model, and the optical axis of the camera. As seen in Figure 2-10, the correct positioning of the rapid prototyped object reduces obstructions in the optical path of both the camera and light sheet and thus results in higher-quality raw PIV data.

To avoid problems using glass spheres $\sim 10 \mu\text{m}$ in diameter, which are typically used in PIV and could potentially become trapped and build up in our complex model, small air bubbles entrained in the viscous index matching fluid were used as seed particles instead. The air bubbles were generated during the filling of the experimental flow loop. Seeding density was controlled by opening the low-pressure side of the pump to atmosphere, thereby allowing the system to entrain outside air. Air that passed through the centrifugal pump impeller were broken up into small bubbles. A similar approach was used by (Chevrin, 1988) & (McPhail, 2012), who found

that air bubbles entrained in a viscous working fluid were superior to the use of small commercially available seeding particles (Chevrin, 1988) & (McPhail, 2012).

It is then necessary to determine whether or not the air bubbles faithfully follow the flow. The Stokes number, which is the dimensionless ratio of the relaxation time of a particle (or air bubble) to the characteristic time scale of the flow (Raffel, et al., 2007), is used as an indicator of whether or not a particle will follow the flow. The Stokes number is defined as

$$Stk = \frac{\tau * U_o}{d_h} \quad (2.16)$$

where

$$\tau = \frac{\rho_{air} * d_p^2}{18 * \mu_{NaI}} \quad (2.17)$$

and U_o is the flow speed, d_h is the hydraulic diameter of the nasal passageway, ρ_{air} is the density of the air bubble, d_p is the diameter of the air bubble, and μ_{NaI} is the kinematic viscosity of the NaI solution.

Gravitational effects were also considered, given that the difference in density between the working fluid and the air bubbles is on the order of 1000. Specifically, as shown by (Zerai, et al., 2005) the settling speed of a small particle in a flow field is given by

$$v_s = \frac{g(\rho_{air} - \rho_{NaI})d_p^2}{18 * \mu_{NaI}} \quad (2.18)$$

where g is the acceleration due gravity and ρ_{NaI} is the density of the working fluid. Substituting values for each of the parameters in Equation 2.18, it can be shown that the settling

speed, v_s , is two orders of magnitude smaller than the minimum measured flow speed in the experiments.

Using the foregoing relationship in equation (2.16) with a custom morphometric image processing code from (Craven, et al., 2007), the Stokes number was analyzed throughout the ten times scaled experimental model. Note that for particles (or air bubbles) to faithfully follow the flow, the Stokes number should be less than 0.1 (Tropea, et al., 2007). Thus, as shown in Figure 2-22, the air bubbles are expected to follow the flow through the nasal airway model and may be used as seeding for PIV measurements.

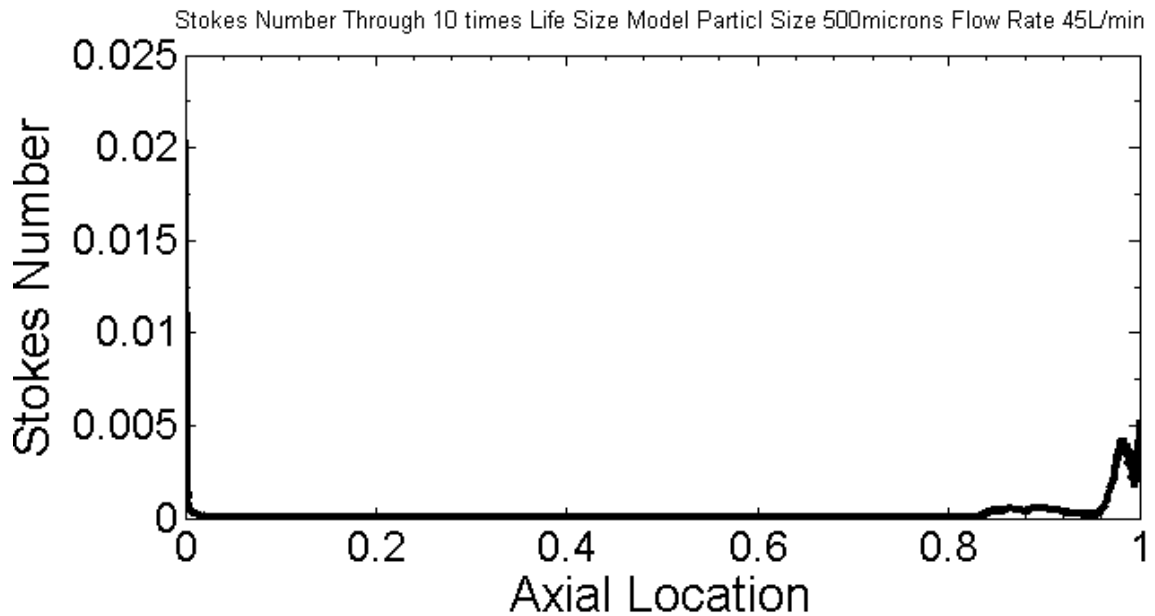


Figure 2-22. Calculation of the Stokes number in the 10 times scaled model of the squirrel nasal airway for a worst-case air bubble size of 500 μm and a flow rate of 45 L/min.

2.2.3.2 Calibration

The procedure of calibrating the PIV data was accomplished by referencing exposed internal geometry in a PIV image pair with the very same plane in the 3D model (Figure 2-24). Magics was used to locate the same landmarks in the 3D model as in the raw PIV images. The in-

plane distance between landmarks was then measured in Magics and used to calibrate the processed displacement PIV data to convert pixel displacement vectors into spatial displacement vectors. The time delay between laser pulses was then used to finally convert the resulting spatial displacement vectors into velocity vectors.

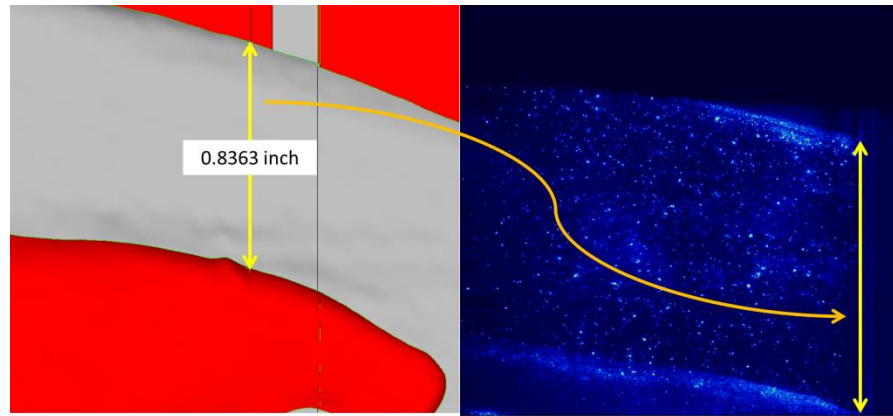


Figure 2-23. PIV calibration. The same spatial landmarks were identified in the PIV images and the digital 3D model. The in-plane distance between the landmarks was then measured in the 3D model and used as the reference length to calibrate the PIV data.

2.2.4 Data Analysis

2.2.4.1 Resistance Curve

Pressure drop across the model was calculated as the difference between static pressure measurements acquired using two separate pressure transducers (see section 2.2.2). The pressure transducers output a DC voltage. The voltages were then converted to pressure via the calibration curve shown in Figure 2-21, which is of the form

$$P = C * V + D \quad (2.19)$$

where P is static pressure, C is the slope, V is voltage output, and D is the linear offset.

The flow rate through the model was simultaneously measured using the flow meter. Pressure drop and flow rate were simultaneously measured across a range of flow rates to obtain the resistance, or flow impedance, curve for the nasal airway model. It is important to note that this resistance curve is for the scaled model of the left nasal airway with NaI solution. To obtain the pressure drop at life size with air as the working fluid, Equation 2.5 may be used.

2.2.4.2 Vector Fields

As stated by LaVision, DaVis 8.0 (LaVision, Germany), is a post processing program that can be used to calculate displacements with a standard Fast Fourier Transform based cross-correlation algorithm. Masks were applied to each region of interest to process areas of only quality data. A 128x128 square pixel interrogation region with a 4:1 elliptical weighting was used on the initial pass. The second and third passes used a window of 64x64 with a 2:1 elliptical weighting. The elliptical weighting provides improved resolution of the velocity gradient. All passes were conducted with an interrogation region overlap of 50%. After each correlation pass, vectors were removed by a median filter if at least one of its components was greater than 3 RMS from the median component of neighboring vectors. Holes in the data were filled with subsequent processed image pair vectors during the averaging of all processed images for each of the regions of interest. Lastly, the first two columns and last two columns of vectors in the field were discarded to avoid problems due to particle entry or exiting between subsequent images.

Chapter 3 Results

3.1 Cases Studied

One of the aims of this study is to create an experimental database of PIV and resistance curve data for flow in a ten times life size model of the nasal airway of the eastern grey squirrel, an extremely complex internal flow passage. This database can then be used to validate CFD simulations using the same model. The resistance curve was measured using the NaI refractive index matching fluid (see properties in Table 2-1). Planar PIV measurements of flow velocity at various locations in the model were then acquired and post-processed (as described in chapter 2) for two flow rate conditions: 10 L/min (Q_{LOW}) and 45 L/min (Q_{HIGH}).

3.1.1 Inspiratory Flow

3.1.1.1 Resistance Curves

Resistance data was collected over several experimental runs, spanning multiple days (Figure 3-1). The flow rates ranged from 0 L/min to 45 L/min, which was determined to be the highest possible flow rate achievable in the system. Measurements were acquired in increments of approximately 4-5 L/min, except below 10 L/min, where smaller increments of 1.0 L/min were used to better resolve the highly-nonlinear region of the resistance curve near the zero flow condition, and where there is also a higher degree of uncertainty in the pressure measurements (Figure 3-2). As shown in Figure 3-1, the resistance data that was collected on different days was found to be repeatable.

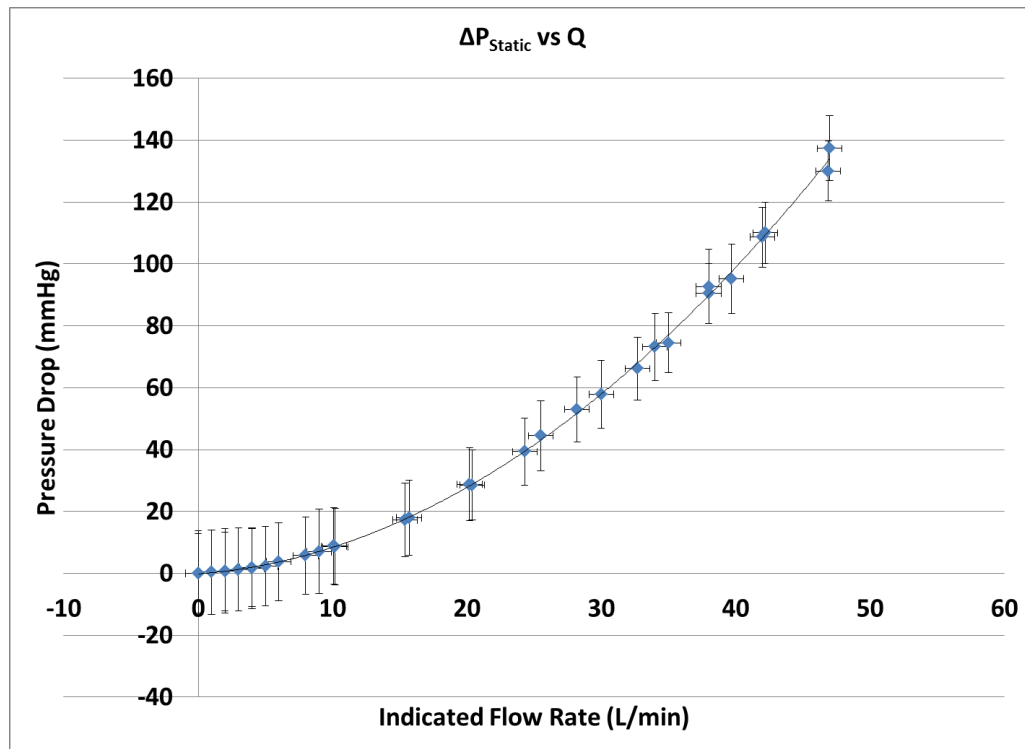


Figure 3-1. Resistance curve for the 10 times scaled model using the NaI refractive index matching fluid the uncertainty bars represent 95% confidence intervals, and were computed using the approach described by (Coleman & Steele, 2009) presented in Appendix B

Uncertainty Analysis. Parabola fit of data yielded $\Delta P = 0.0539Q^2 + 0.3214Q - 0.1741$; $R^2 = 0.9991$.

3.1.1.2 PIV Measurements

PIV data was acquired in the 10 times scaled model under two steady flow rate conditions: Q_{LOW} (10 L/min) and Q_{HIGH} (45 L/min), at six different locations in the model at each flow rate. The particular locations were in several anatomical regions of interest (dorsal meatus, nasomaxillary region, and nasopharynx) and in multiple sagittal plans (see Figure 3-2). The resulting PIV velocity fields at each flow rate are shown in Figures 3-4 and 3-5.

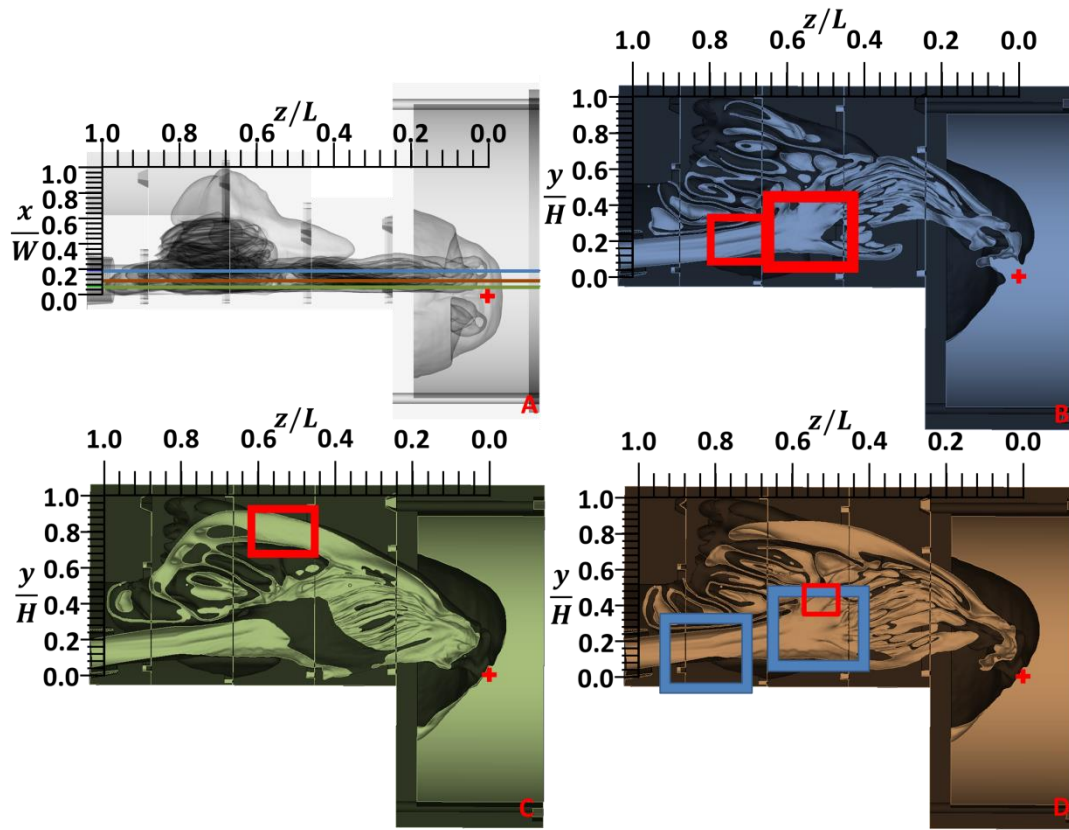


Figure 3-2. PIV measurement locations. A) Top view of a transparent 3-D rendering of the model with colored lines showing the orientation of the monochromatically colored sagittal planes displayed in B-D, where both the size and location of the PIV fields of view are shown. ($X_B/W = 0.181$, $X_C/W = 0.0548$, $X_D/W = 0.108$)

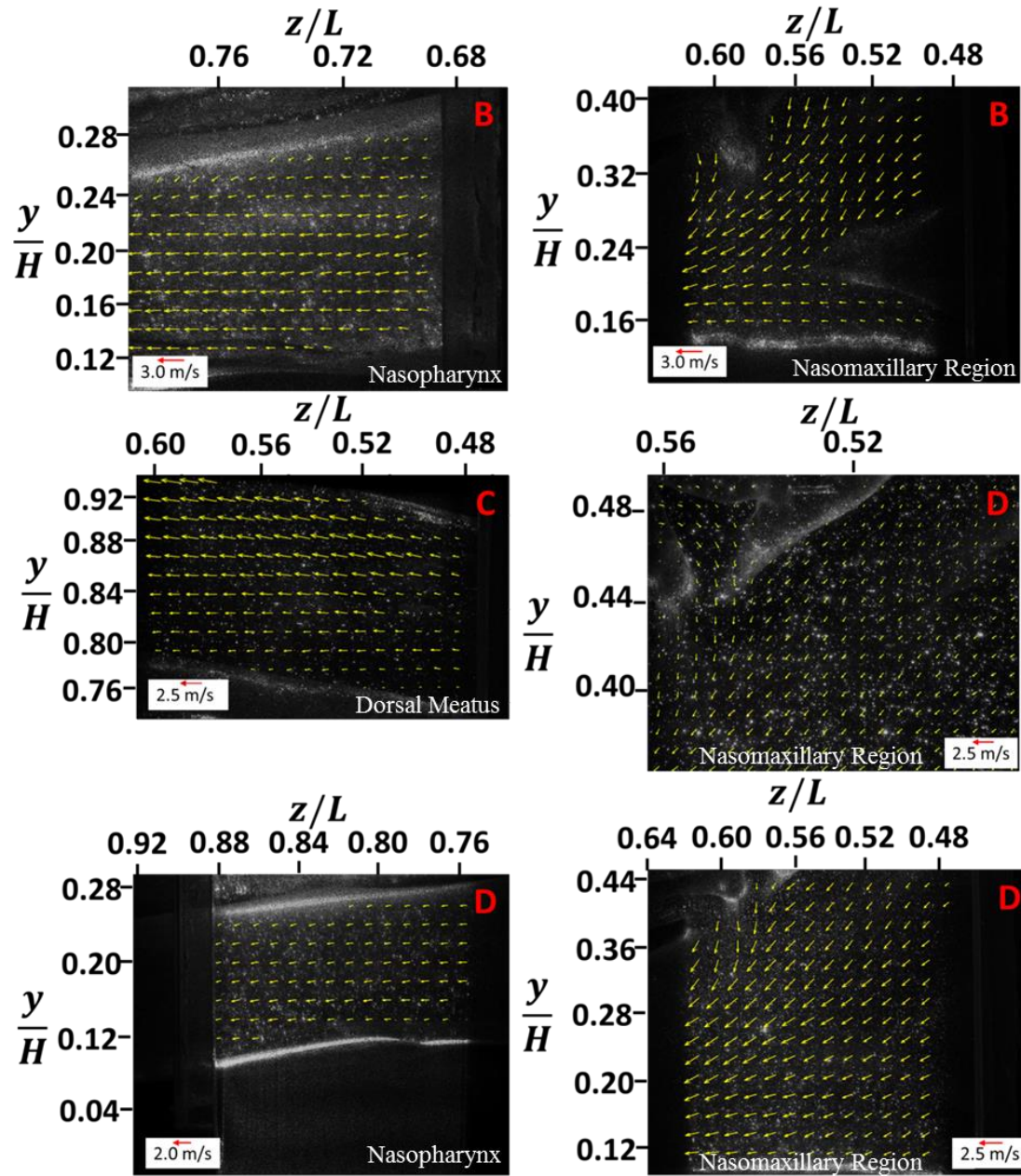


Figure 3-3. PIV velocity vectors at a flow rate of 45 L/min (Q_{HIGH}). Red letters indicate the corresponding sagittal plane shown in Figure 3-2. Vectors in every other row and every other column have been omitted for display purposes.

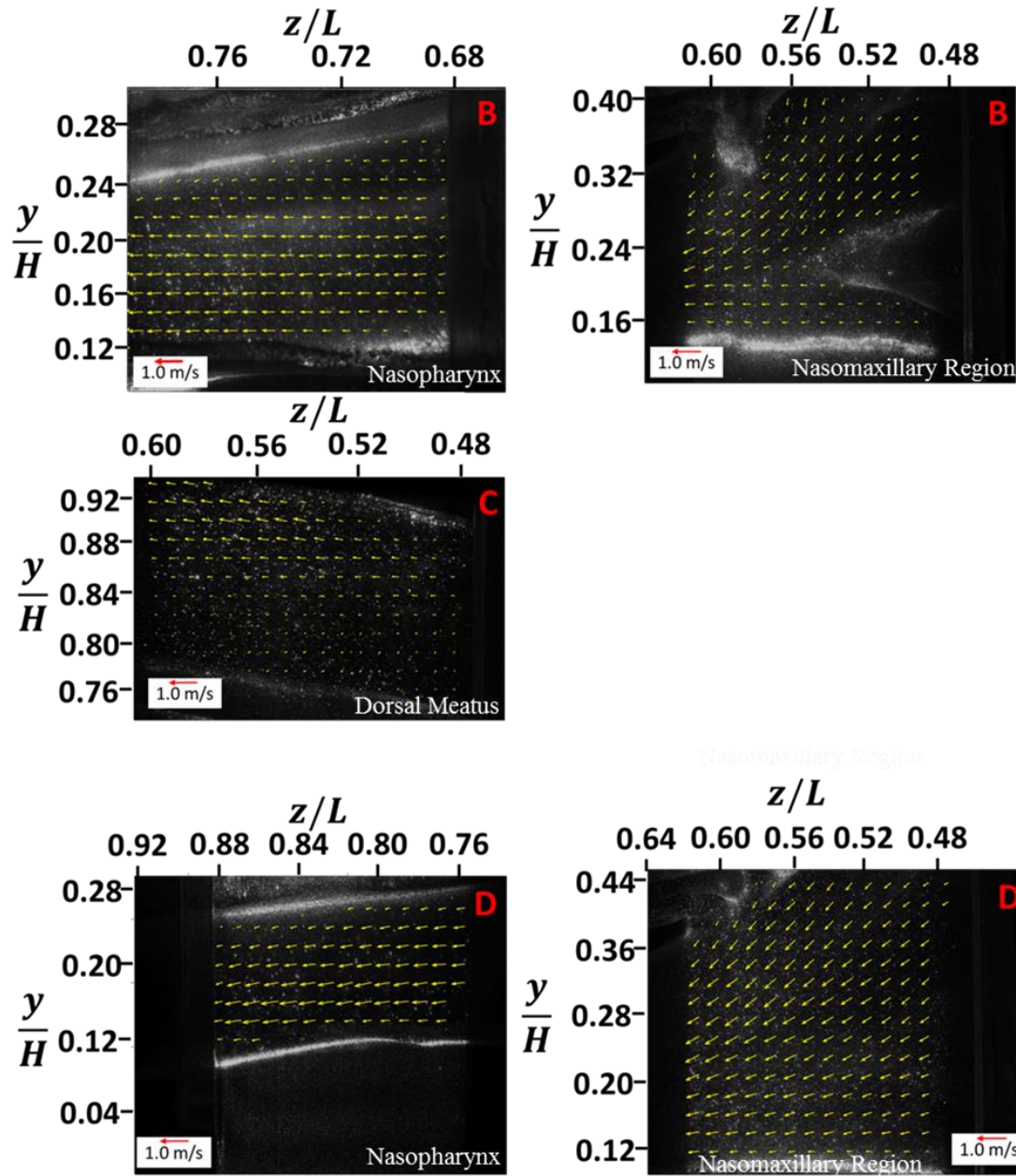


Figure 3-4. PIV velocity vectors at a flow rate of 10 L/min (Q_{LOW}). Red letters indicate the corresponding sagittal plane shown in Figure 3-2. Vectors in every other row and every other column have been omitted for display purposes.

Chapter 4

Summary and Conclusions

4.1 Summary of Results

The objective of this research was to create an anatomically accurate experimental model of a complex rodent nasal airway and to acquire PIV measurements in the model for CFD validation. The results of this work are intended to contribute to the fundamental understanding of nasal form and function in mammals, and to advance current state-of-the-art optical flow measurement techniques (PIV in particular) in complex experimental models.

An anatomically-accurate ten times scale model of the left nasal airway of the eastern gray squirrel was successfully manufactured using SLA rapid prototyping and a NaI solution with the same index of refraction as the SLA material was created. PPIV measurements were then successfully acquired in the refractive index-matched model. Flow seeding with conventional glass spheres was found to be problematic in complex regions of the model due to particle deposition and buildup. Instead, air bubbles entrained in the viscous NaI solution were used as seed for PIV. The resulting experimental database may be used for validation of CFD simulations of laminar flow in complex internal flow passageways.

4.2 Recommendations for Future Work

To build on the present study, future work might include the three-dimensional characterization of the internal flow in the nasal passageway via stereoscopic particle image velocimetry (SPIV). It is possible to acquire SPIV measurements in the model that was used in

this study, but a more complicated method of calibration is required due to the fact that the imaging plane no longer has a uniform magnification factor across it. This non-uniform magnification requires a more complex, three-dimensional calibration methodology. Though three-dimensional calibration targets are available, for the present complex internal nasal passageway, such calibration targets will not fit inside the model. However, a similar approach used to calibrate the present planar PIV measurements might be used, where known anatomical landmarks in the 3-D model are identified in the raw SPIV images and used to develop a three-dimensional calibration.

Bibliography

Becker, R. & King, J., 1957. Delineation of the nasal air streams in the living dog. *AMA Arch Otolaryngol*, pp. 428-436.

Bell, S., 2001. *A beginner's guide to uncertainty of measurement*, Teddington: Crown.

Budwig, R., 1994. Refractive index matching methods for liquid flow investigations. *Experiments in Fluids*, pp. 350-355.

Butscher, D., Hutter, C. & Kuhn, S., 2012. Particle image velocimetry in a foam-like porous structure using refractive index matching: a method to characterize the hydrodynamic performance of porous structures. *Experiments in Fluids*, pp. 53:1123-32.

Canstein, C. et al., 2008. 3D MR flow analysis in realistic rapid-prototyping model systems of the thoracic aorta: comparison with in vivo data and computational fluid dynamics in identical vessel geometries. *Magn Reson Med*, pp. 535-546.

Cheng, Y. et al., 1990. Deposition of ultrafine aerosols in rat nasal molds. *Toxicology and applied pharmacology*, pp. 222-233.

Chevrin, P.-A., 1988. *The structure of Reynolds stress in near wall region of a turbulent pipe flow*, University Park: The Pennsylvania State University.

Chung, S. & Kim, S., 2008. Digital particle image velocimetry studies of nasal airflow. *Respiratory physiology & neurobiology*, pp. 111-120.

Coleman, H. W. & Steele, G. W., 2009. *Experimentation, validation, and uncertainty analysis for engineers*. s.l.:John Wiley & Sons.

Craven, B. A. et al., 2007. Reconstruction and morphometric analysis of the nasal airway of the dog (*canis familiaris*) and implications regarding olfactory airflow. *The Anatomical Record*, pp. 1325-40.

Craven, B., Paterson, E. & Settles, G., 2009a. The fluid dynamics of canine olfaction: a new explanation for macrosmia. *J Royal Society Interface*, pp. 1-11.

Craven, B., Paterson, E. & Settles, G., 2010. The fluid dynamics of canine olfaction: unique nasal airflow patterns as an explanation of macrosmia. *J. R. Soc. Interface*, pp. 933-43.

Craven, B., Paterson, E., Settles, G. & Lawson, M., 2009b. Development and verification of a high-fidelity computational fluid dynamics model of canine nasal airflow. *J Biomech Eng*, p. 131: 091002.

Dawes, J., 1952. The course of the nasal airstreams.. *J Laryngol Otol*, pp. 583-593.

De Rycke, L. M. et al., 2003. Magnetic resonance imaging, computed tomography, and cross-sectional views of the anatomy of normal nasal cavities and paranasal sinuses in mesaticephalic dogs. *American journal of veterinary research*, pp. 1093-1098.

de Zélicourt, D. et al., 2005. Singlestep stereolithography of complex anatomical models for optical flow measurements. *J Biomech Eng*, pp. 204-207.

Doorly, D., Taylor, D. & Schroter, R., 2008. Mechanics of airflow in the human nasal airways. *Respiratory Physiology & Neurobiology*, pp. 100-110.

Elkins, C. & Alley, M., 2007. Magnetic resonance velocimetry: applications of magnetic resonance imaging in the measurement of fluid motion. *Experiments in Fluids*, pp. 823-858.

Ereaut, P., 2011. *Thermopedia*. [Online]
Available at: www.thermopedia.com/content/1201/
[Accessed 2 December 2012].

Hendriks, F. & Aviram, A., 1982. Use of zinc iodide solutions in flow research. *AIP Review of Scientific Instruments*, pp. 75-78.

Hole, G., 2014. *warren pumps*. [Online]
Available at: [www.warrenpumps.com/brochures/Fluid Viscosity Effects.PDF](http://www.warrenpumps.com/brochures/Fluid%20Viscosity%20Effects.PDF)
[Accessed 28 5 2014].

- Hopkins, L., Kelly, J., Wexler, A. & Prasad, A., 2000. Particle image velocimetry measurements in complex geometries. *Experiments in Fluids*, pp. 91-95.
- Hornung, D. et al., 1987. Airflow patterns in a human nasal model. *Arch Otolaryngol Head Neck Surg*, pp. 169-172.
- Kelly, J. K. J. A. B., 2001b. Desposition of fine and coarse aerosols in a rat nasal mold. *Inhalation Toxicology*, pp. 577-588.
- Kimbell, J. et al., 1997. Computer simulation of inspiratory airflow in all regions of the F344 rat nasal passages. *Toxicol Appl Pharmacol*, pp. 388-398.
- Kimbell, J. et al., 1993. Application of computational fluid dynamics to regional dosimetry of inhaled chemicals in the upper respiratory tract of the rat. *Toxicol Appl Pharmacol*, pp. 253-263.
- Kimbell, J. et al., 2001. Dosimetry modeling of inhaled formaldehyde: comparisons of local flux predictions in the rat, monkey, and human nasal passages. *Toxicol Sci*, pp. 100-110.
- Lawson, M. J., 2010. *A fundamental study of the airflow and odorant transport phenomena of canine olfaction*, University Park: The Pennsylvania State University.
- Liu, Y. et al., 2009. Creation of a standardized geometry of the human nasal cavity. *Journal of applied physiology*, p. 106: 784.
- Lorensen, W. E. & Cline, H. E., 1987. Marching cubes: A high resolution 3D surface construction algorithm. *ACM Siggraph Computer Graphics*, p. Vol. 21. No. 4.
- McPhail, M., 2012. *Multicolor particle shadow velocimetry and accelerometry for measurements in a human airway model*, University Park: The Pennsylvania State University.
- Morgan, K. et al., 1991. Studies of inspiratory airflow patterns in the nasal passages of the F344 rat and rhesus monkey using nasal molds: relevance to formaldehyde toxicity. *Toxicol Appl Pharmacol*, pp. 223-240.

Morgan, K. & Monticello, T., 1990. Airflow, gas deposition, and lesion distribution in the nasal passages. *Environ Health Perspect*, pp. 209-218.

Narrow et al, T., 2000-03. A simple model for the refractive index sodium iodide aqueous solutions. *Experiments in fluids*, pp. 282-283.

Negus, V., 1958. *The comparative anatomy and physiology of the nose and paranasal sinuses*. London: Livingstone.

Patra, A., Gooya, A. & Morgan, K., 1986. Airflow characteristics in a baboon nasal passage cast. *J Appl Physiol*, pp. 1959-1966.

Raffel, M., Willert, C., Wereley, C. & Kompenhans, J., 2007. *Particle image velocimetry: a practical guide*. Berlin: Springer.

Ranslow, A. N. et al., 2014. Reconstruction and morphometric analysis of the nasal airway of the white-tailed deer (*Odocoileus virginianus*) and implications regarding respiratory and olfactory airflow. *The Anatomical Record*, p. n/a.

Richter, J. P. et al., n.d. Reconstruction and morphometric analysis of the nasal airway of the eastern grey squirrel (*Sciurus carolinensis*) and implications regarding respiratory and olfactory airflow. *in preparation*.

Schroeter et al, J. D., 2012-01. Computational fluid dynamics simulations of submicrometer and micrometer particle deposition in the nasal passages of a Sprague-Dawley rat. *Journal of aerosol science*, pp. 31-44.

Taubin, G., 1995. *Curve and surface smoothing without shrinkage*. Cambridge, MA, IEEE.

Tropea, C., Yarin, A. L. & Foss, J. F., 2007. *Springer handbook of experimental fluid mechanics*. Berlin: Springer.

Weishaupt, D., Köchli, V. D. & Marincek, B., 2003. *How does MRI work?*. Berlin: Springer.

Yang, G., Scherer, P. & Mozell, M., 2007a. Modeling inspiratory and expiratory steady-state velocity fields in the Sprague-Dawley rat nasal cavity. *Chem Senses*, pp. 215-223.

Zerai, B. et al., 2005. Flow characterization through a network cell using particle image velocimetry. *Transport in porous media*, pp. 159-181.

Zhao, K., Dalton, P., Yang, G. & Scherer, P., 2006. Numerical modeling of turbulent and laminar airflow and odorant transport during sniffing in the human and rat nose. *Chem Senses*, pp. 107-118.

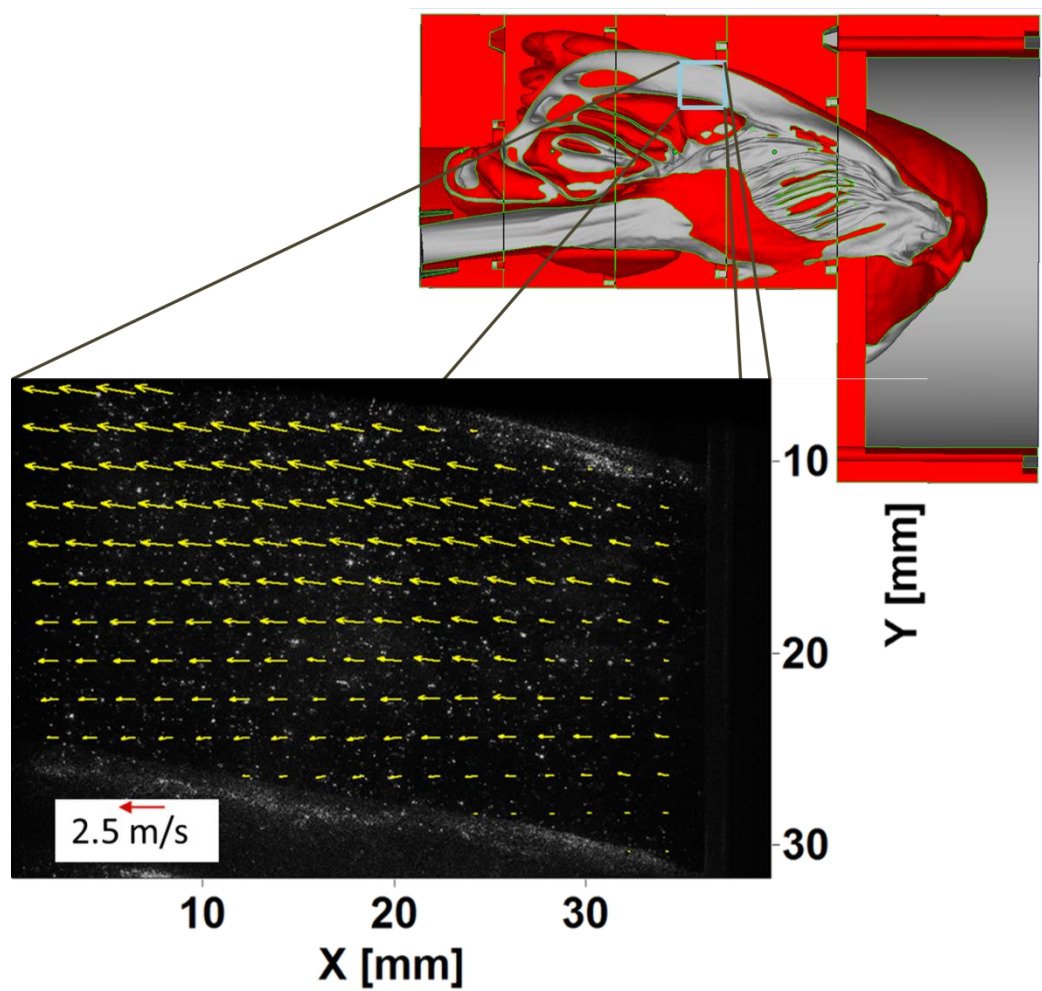
*Appendix A***Alternative PPIV Data Presentation**

Figure A-1. PIV velocity vectors in the dorsal meatus at a flow rate of 45 L/min in a sagittal plane located at $X_C/W = 0.0548$ (see Figure 3-2).

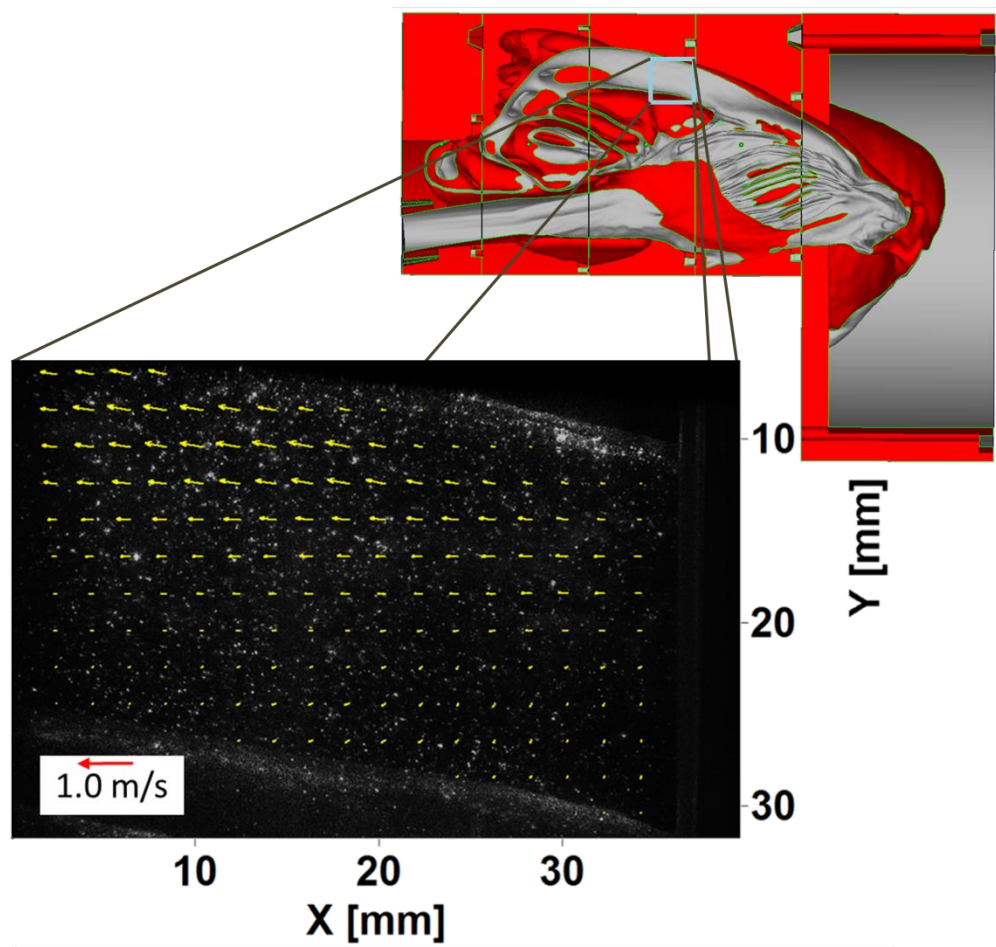


Figure A-2. PIV velocity vectors in the dorsal meatus at a flow rate of 10 L/min in a sagittal plane located at $X_C/W = 0.0548$ (see Figure 3-2).

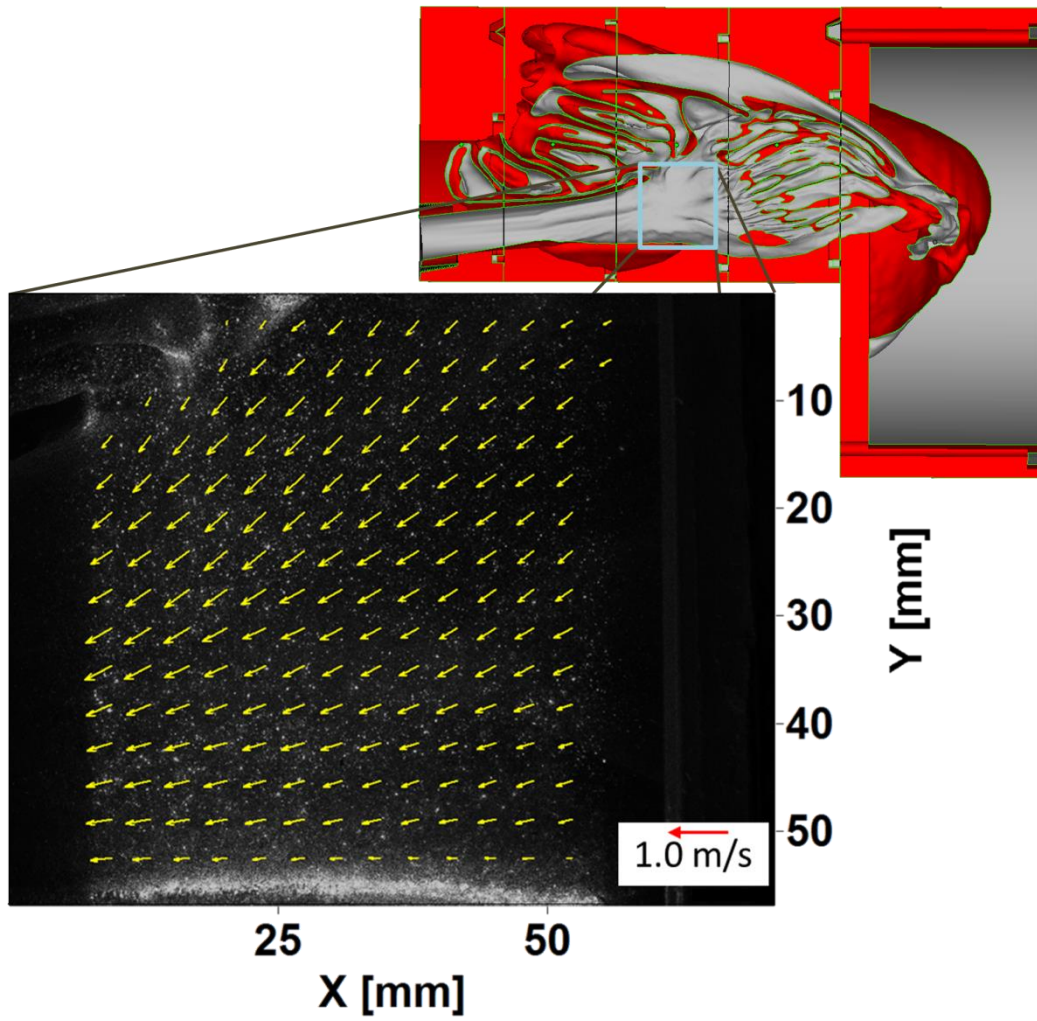


Figure A-3. PIV velocity vectors in the entrance to the Nasopharynx at a flow rate of 10 L/min in a sagittal plane located at $X_D/W = 0.108$ (see Figure 3-2).

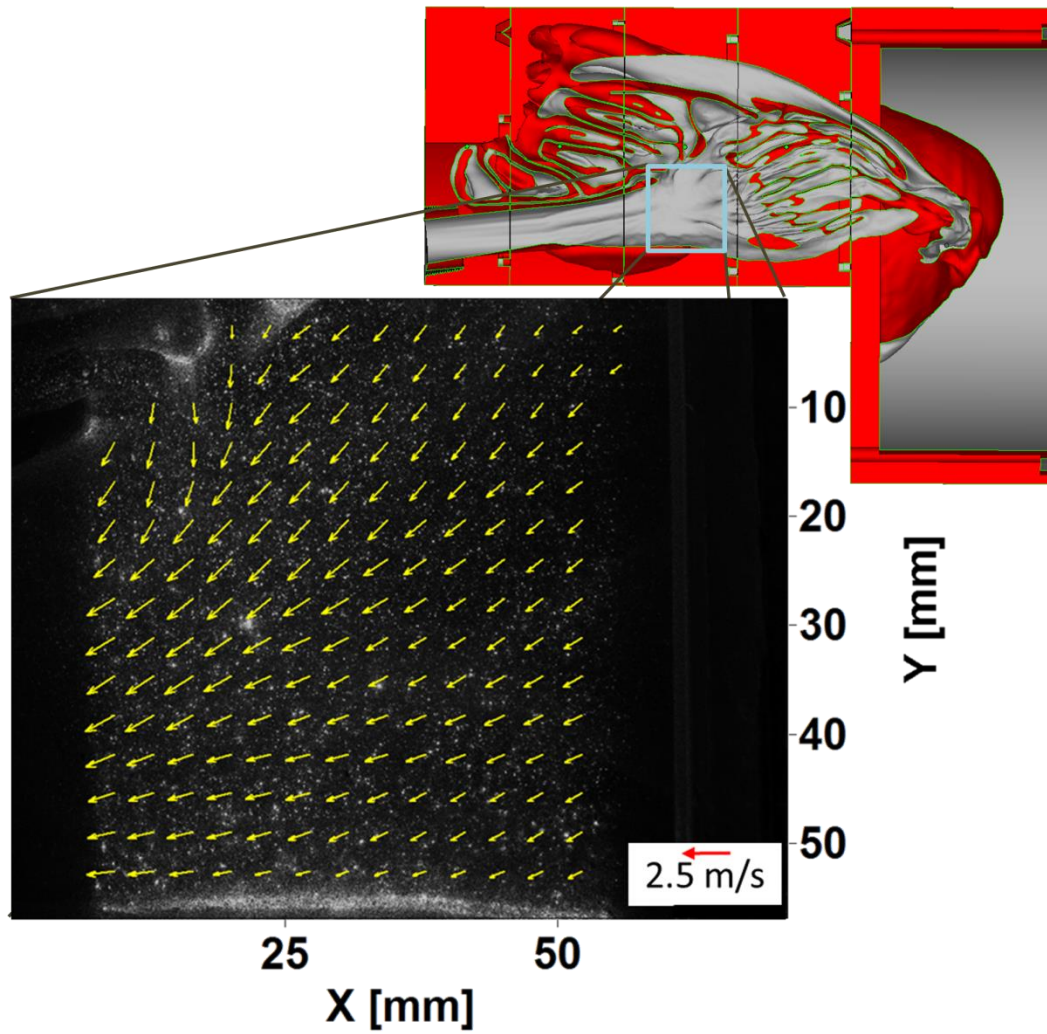


Figure A-4. PIV velocity vectors in the entrance to the Nasopharynx at a flow rate of 45 L/min in a sagittal plane located at $X_D/W = 0.108$ (see Figure 3-2).

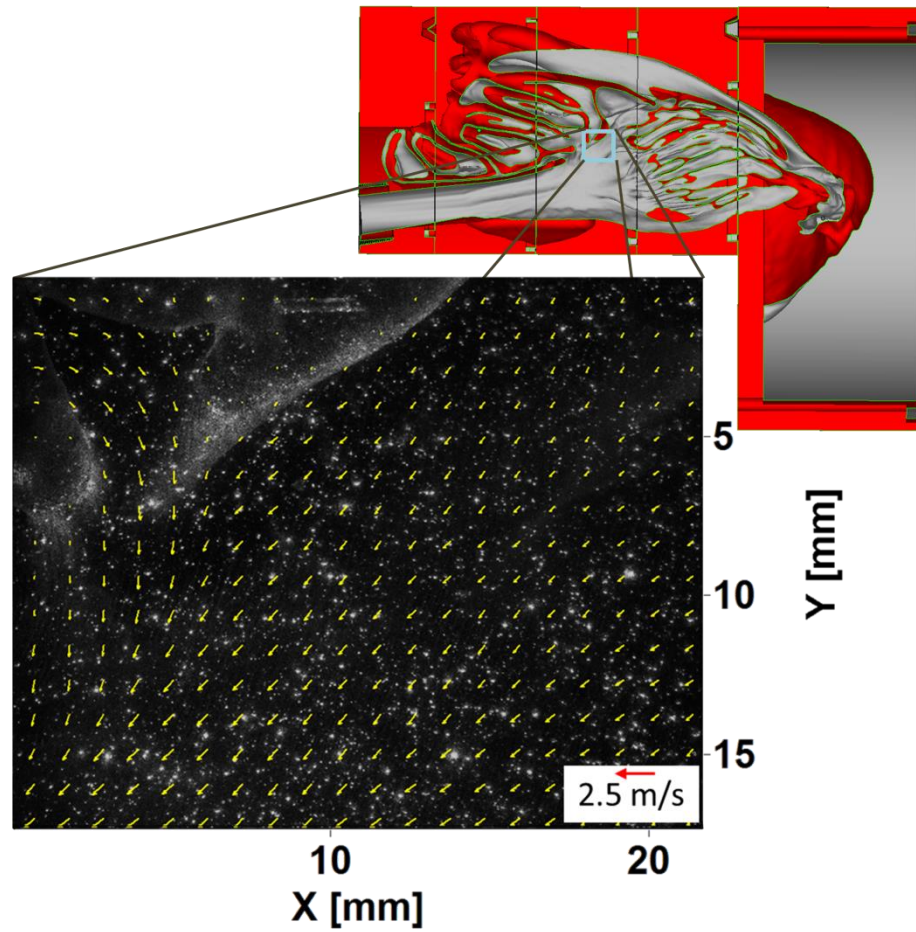


Figure A-5. PIV velocity vectors in the entrance to the Nasopharynx at a flow rate of 45 L/min in a sagittal plane located at $X_D/W = 0.108$ (see Figure 3-2).

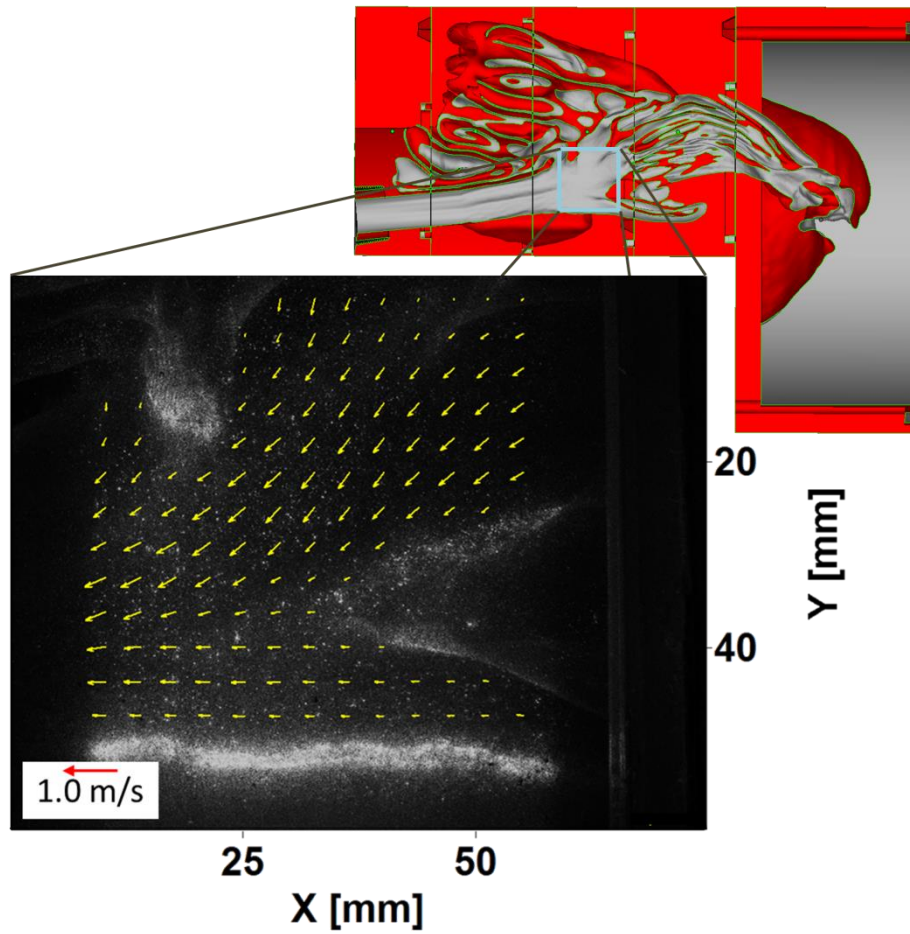


Figure A-6. PIV velocity vectors in the entrance to the Nasopharynx at a flow rate of 10 L/min in a sagittal plane located at $X_B/W = 0.181$ (see Figure 3-2).

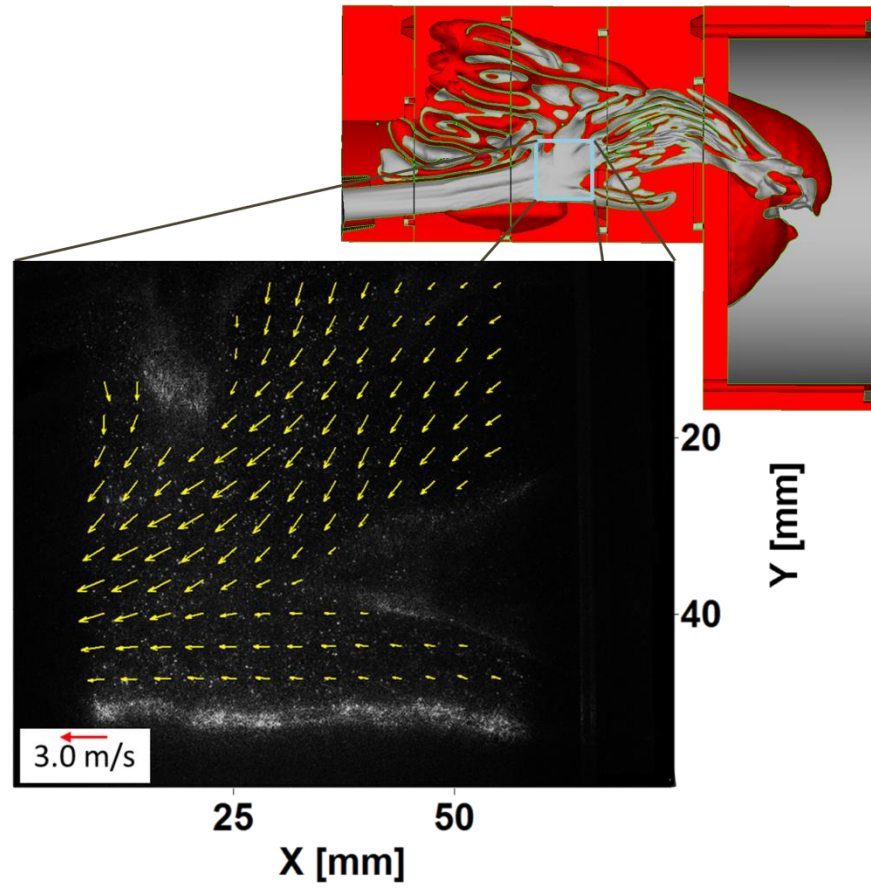


Figure A-7. PIV velocity vectors in the entrance to the Nasopharynx at a flow rate of 45 L/min in a sagittal plane located at $X_B/W = 0.181$ (see Figure 3-2).

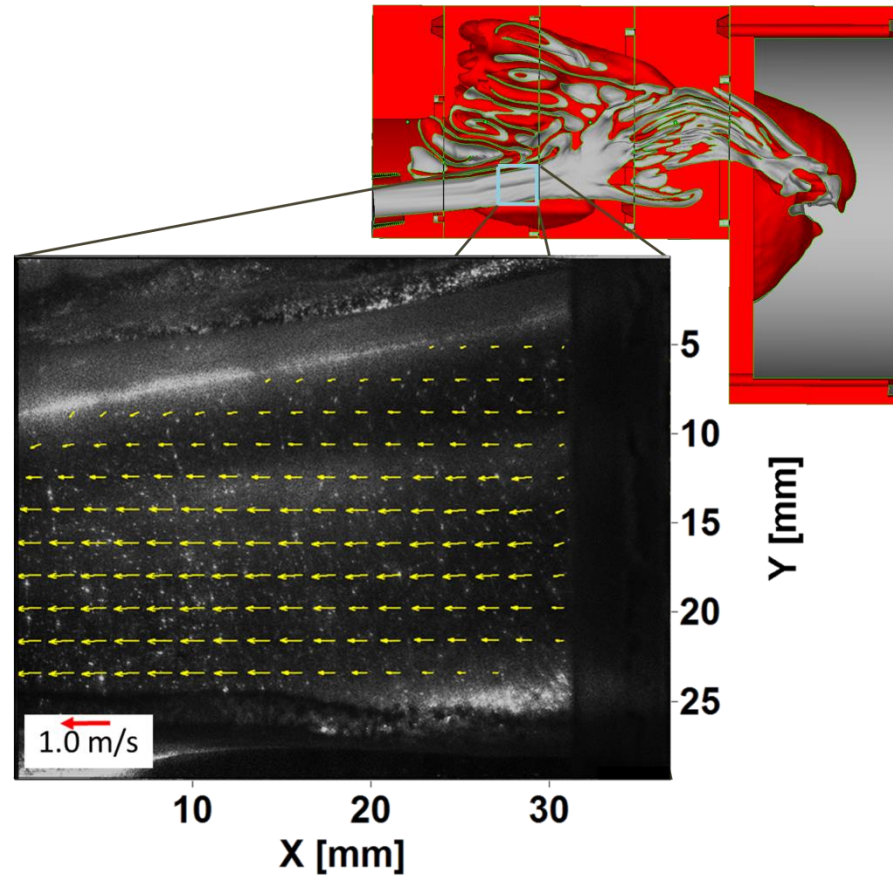


Figure A-8. PIV velocity vectors in the beginning of the Nasopharynx at a flow rate of 10 L/min in a sagittal plane located at $X_B/W = 0.181$ (see Figure 3-2).

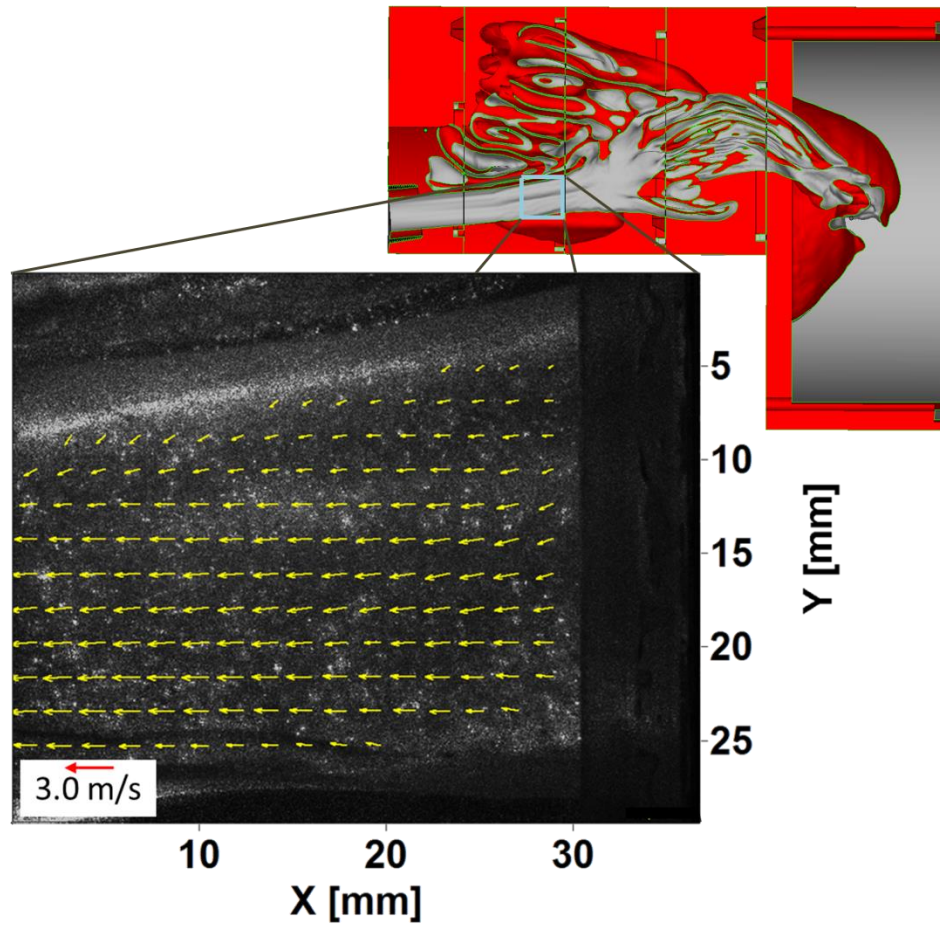


Figure A-9. PIV velocity vectors in the beginning of the Nasopharynx at a flow rate of 45 L/min in a sagittal plane located at $X_B/W = 0.181$ (see Figure 3-2).

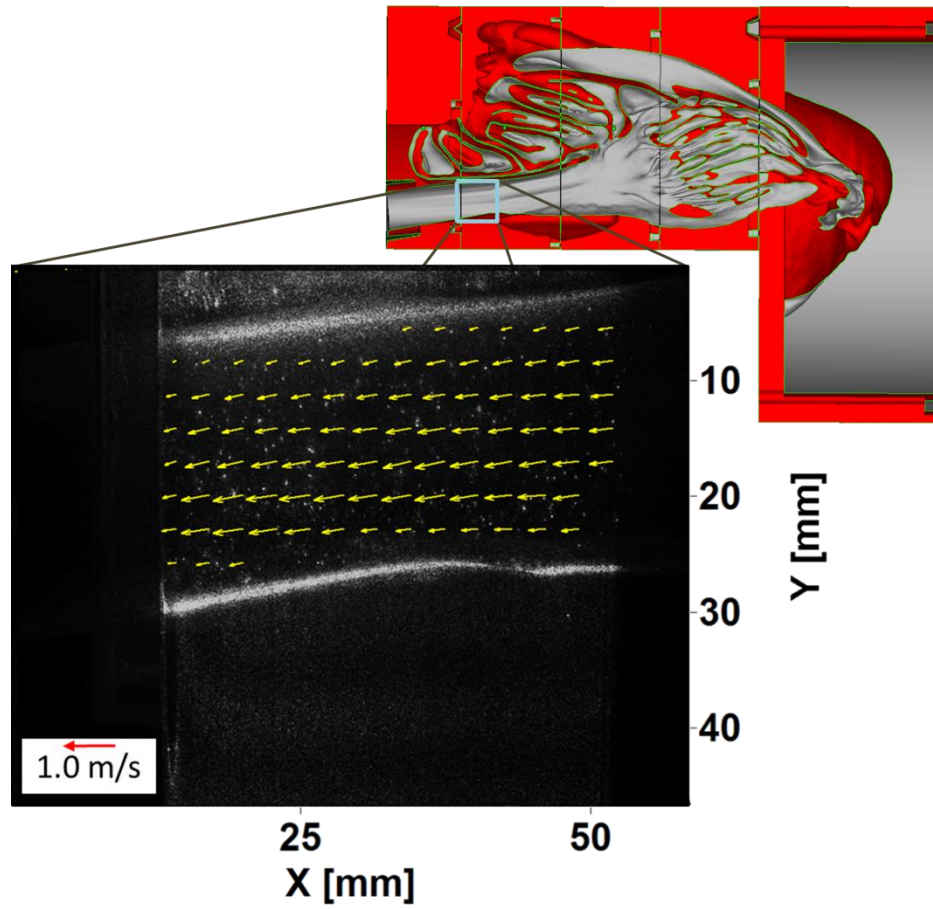


Figure A-10. PIV velocity vectors in the end of the Nasopharynx at a flow rate of 10 L/min in a sagittal plane located at $X_D/W = 0.108$ (see Figure 3-2).

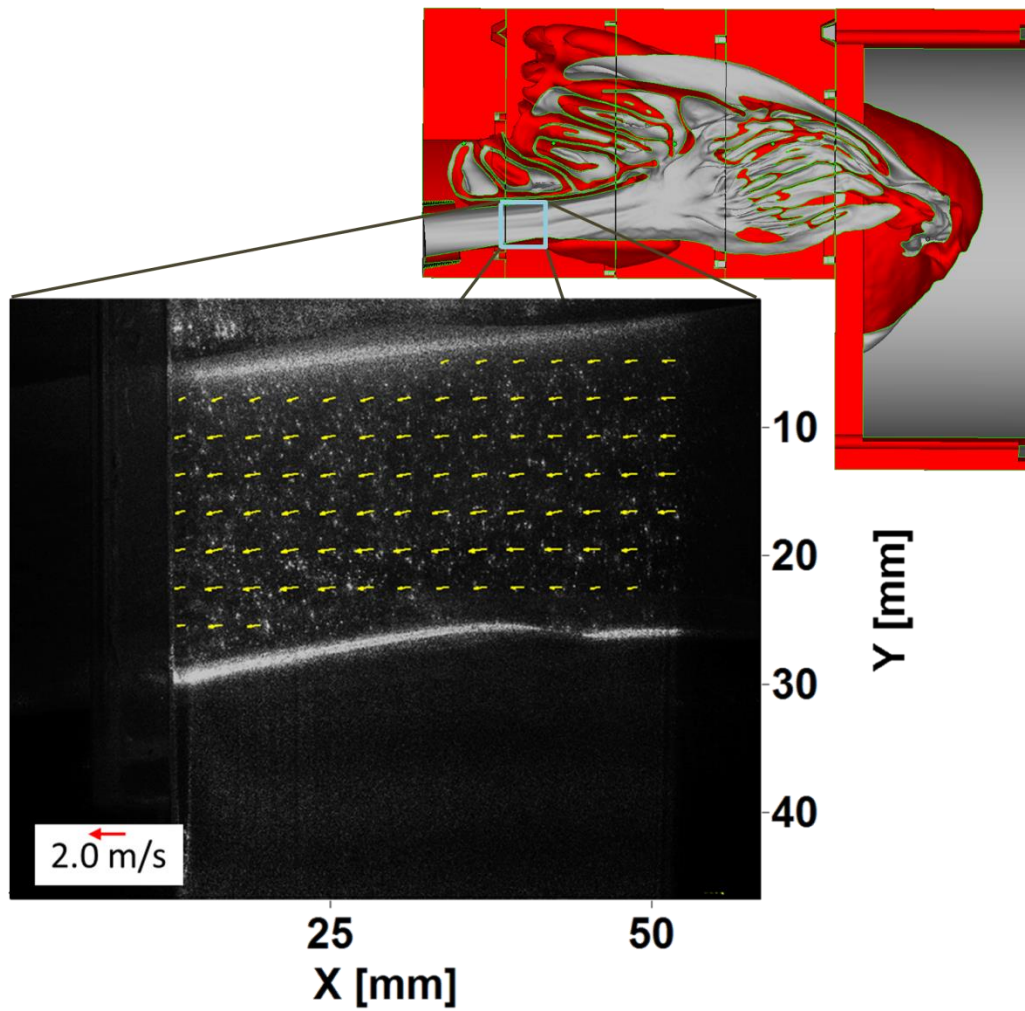


Figure A-11. PIV velocity vectors in the end of the Nasopharynx at a flow rate of 45 L/min in a sagittal plane located at $X_D/W = 0.108$ (see Figure 3-2).

Appendix B

Uncertainty Analysis

B.1 Theory

The uncertainty analysis techniques used for resistance curve result is presented here. A practical approach was taken where conservative values of measurement uncertainties were estimated. First the general forms of the uncertainty equations are shown, followed by the separate treatment of the uncertainty of each measurement taken for resistance curve data. The uncertainty analysis closely follows the Taylor series method presented in (Coleman & Steele, 2009). A general data reduction equation for an experimental result y , as a function of k measured variables is shown by,

$$y = y(x_1, x_2, \dots, x_k). \quad (\text{B.1})$$

The combined standard uncertainty, ε_y , is given by the root-sum-square of the systematic (bias), b_y , and random (precision) uncertainties, s_y , of the measurement, hence

$$\varepsilon_y = \sqrt{b_y^2 + s_y^2}. \quad (\text{B.2})$$

The systematic uncertainties are defined as

$$b_y^2 = \sum_{i=1}^k \left(\frac{\partial y}{\partial x_i} \right)^2 b_{xi}^2 \quad (\text{B.3})$$

where b_{xi} are the systematic uncertainties of each measured variable, and $\frac{\partial y}{\partial x_i}$ are the sensitivity coefficients. The random uncertainty is defined similarly as

$$s_y^2 = \sum_{i=1}^k \left(\frac{\partial y}{\partial x_i} \right)^2 s_{xi}^2 \quad (\text{B.4})$$

A coverage factor is applied to the combined standard uncertainty to provide an estimate of the expanded uncertainty, shown in equation (B.5). For this work, error distributions were considered Gaussian with the t-distribution chosen to give 95% level of confidence in

$$E_y = 1.96 \varepsilon_y \quad (\text{B.5})$$

For repeated measurements, the random uncertainty should not be estimated at the elemental level, as advised by (Coleman & Steele, 2009). For the presentation of mean quantities, the random uncertainty is estimated by

$$s_y^2 = \frac{\sigma_y^2}{N} \quad (\text{B.6})$$

where σ_y^2 is the variance of N samples, shown in equation (B.7).

$$\sigma_y^2 = \frac{1}{N} \sum_{m=1}^N (y_m - \bar{y})^2 \quad (\text{B.7})$$

B.2 Pressure drop

From equation (2.19), relative uncertainty as stated by (Bell, 2001) dictates that

$$\frac{u(P)}{P} = \sqrt{\left(\frac{u(C)}{C}\right)^2 + \left(\frac{u(V)}{V}\right)^2} \quad (\text{B.8})$$

where $u(P)$, $u(C)$, and $u(V)$ represent Type A standard of uncertainty for pressure, calibration factor, and voltage respectively.

Voltage drift of the pressure transducers was also characterized and included in uncertainty. Once the system (i.e. amplifier & transducer) was warmed up, it was determined that an elapsed time of 15 minutes was required to reach a steady voltage output. It was at this point when the voltage output values were calibrated for pressure measurements.

B.3 Flow Rate

It was assumed that the calibration parameters given by Transonic Systems were normally distributed, and so equation (B.9) was used to calculate the standard uncertainty in the flow rate measurement

$$\sigma_a = \frac{\mathbf{a}}{2} \quad (\text{B.9})$$

where \mathbf{a} is the calibration uncertainty and this case is equal to 0.5 L/min.